

AperTO - Archivio Istituzionale Open Access dell'Università di Torino

## Influences of urban fabric on pyroclastic density currents at Pompeii (Italy): 1. Flow direction and deposition

### This is the author's manuscript

*Original Citation:*

*Availability:*

This version is available <http://hdl.handle.net/2318/100710> since

*Publisher:*

American Geophysical Union:2000 Florida Avenue Northwest:Washington, DC 20009:(800)966-2481,

*Published version:*

DOI:10.1029/2006JB004444

*Terms of use:*

Open Access

Anyone can freely access the full text of works made available as "Open Access". Works made available under a Creative Commons license can be used according to the terms and conditions of said license. Use of all other works requires consent of the right holder (author or publisher) if not exempted from copyright protection by the applicable law.

(Article begins on next page)

# Influences of urban fabric on pyroclastic density currents at Pompeii (Italy):

## 1. Flow direction and deposition

L. Gurioli,<sup>1,2</sup> E. Zanella,<sup>3,4</sup> M. T. Pareschi,<sup>1</sup> and R. Lanza<sup>3,4</sup>

Received 12 April 2006; revised 12 December 2006; accepted 4 January 2007; published 30 May 2007.

[1] To assess ways in which the products of explosive eruptions interact with human settlements, we performed volcanological and rock magnetic analyses on the deposits of the A.D. 79 eruption at the Pompeii excavations (Italy). During this eruption the Roman town of Pompeii was covered by 2.5 m of fallout pumice and then partially destroyed by pyroclastic density currents (PDCs). Anisotropy of magnetic susceptibility measurements performed on the fine matrix of the deposits allowed the quantification of the variations in flow direction and emplacement mechanisms of the parental PDCs that entered the town. These results, integrated with volcanological field investigations, revealed that the presence of buildings, still protruding through the fallout deposits, strongly affected the distribution and accumulation of the erupted products. All of the PDCs that entered the town, even the most dilute ones, were density stratified currents in which interaction with the urban fabric occurred in the lower part of the current. The degree of interaction varied mainly as a function of obstacle height and density stratification within the current. For examples, the lower part of the EU4pf current left deposits up to 3 m thick and was able to interact with 2- to 4-m-high obstacles. However, a decrease in thickness and grain size of the deposits across the town indicates that even though the upper portion of the current was able to decouple from the lower portion, enabling it to flow over the town, it was not able to fully restore the sediment supply to the lower portion in order to maintain the deposition observed upon entry into the town.

**Citation:** Gurioli, L., E. Zanella, M. T. Pareschi, and R. Lanza (2007), Influences of urban fabric on pyroclastic density currents at Pompeii (Italy): 1. Flow direction and deposition, *J. Geophys. Res.*, 112, B05213, doi:10.1029/2006JB004444.

## 1. Introduction

[2] During the A.D. 79 eruption of Vesuvius, the Roman town of Pompeii, 9 km southeast of the vent, was first covered by 2.5 m of fall deposits before being partially destroyed by a series of pyroclastic density currents (Figure 1a). Pyroclastic density currents (PDCs) are stratified currents of solid volcanic debris and gases, at temperatures of hundreds of degrees Celsius and capable of traveling for many kilometers at velocities of tens to hundreds of meters per second [e.g., Freundt and Bursik, 1998; Druitt, 1998; Branney and Kokelaar, 2002]. During the last three centuries, PDCs have been responsible for the deaths of thousands of people and the destructions of entire towns [Blong, 1984; Tanguy et al., 1998]. Although still extremely hazardous in their distal areas, PDCs often leave only very thin deposits in remote locations. Here, their destructive power derives from their high content of very

fine ash, their high velocity and/or their high temperature [Baxter et al., 1998]. Pompeii is located in the medial-to-distal zone of the A.D. 79 deposits (Figure 1a), so the PDC deposits at this location offer a valuable opportunity to examine the thin ash deposits that were emplaced by distal dilute and turbulent ash clouds as they moved through a town [e.g., Sigurdsson et al., 1985; Cioni et al., 1992, 2000]. In addition, the meter-thick massive-to-stratified deposits left by the most energetic and turbulent PDC of the eruption can be examined. This current, related to the onset of the caldera collapse, was sufficiently energetic to knock down walls [e.g., Sigurdsson et al., 1985; Cioni et al., 1992, 2000]. The effects of, and damage caused by, the A.D. 79 eruption on urban settlements have been well documented in a number of recent studies. These have been based on observations of the deposits [e.g., Sigurdsson et al., 1985; Dal Maso et al., 1999; Cioni et al., 2000; Luongo et al., 2003a, 2003b], field surveys of the effects of the eruption on a few buildings [Nunziante et al., 2003], application of numerical models [Dobran et al., 1994; Baxter et al., 1998], and integration of rock magnetic measurements and field observations [Gurioli et al., 2002, 2005]. Interesting parallel observations have been also recently presented regarding the impacts of pyroclastic

<sup>1</sup>Istituto Nazionale di Geofisica e Vulcanologia, Pisa, Italy.

<sup>2</sup>Now at Geology and Geophysics, University of Hawaii, Honolulu, Hawaii, USA.

<sup>3</sup>Dipartimento di Scienze della Terra, Università di Torino, Torino, Italy.

<sup>4</sup>Alpine Laboratory of Paleomagnetism, Peveragno, Italy.

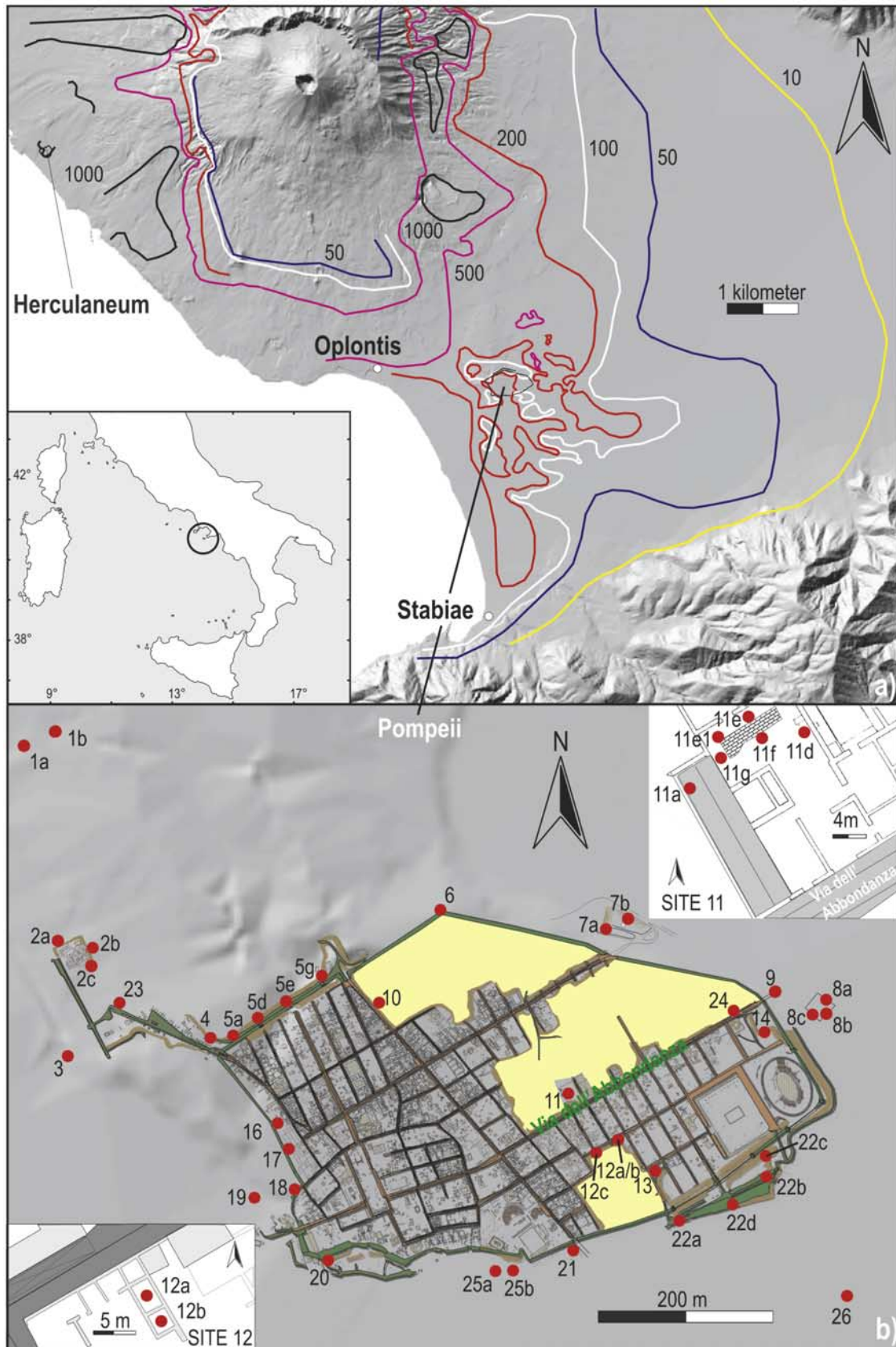


Figure 1



surges on buildings during the eruption of the Soufriere Hills volcano, Montserrat [Baxter *et al.*, 2005].

[3] In this paper the variations in both flow direction and deposition apparent in PDCs entering Pompeii during the A.D. 79 eruption are reported. These results have been obtained from detailed descriptions and measurements within deposits out cropping within and around the archaeological ruins of Pompeii (Figure 1b). Since the Roman ruins of Pompeii were discovered in the 18<sup>th</sup> century, archaeologists have removed great quantities of the deposit during excavations. However, about one third of the ruins still remain buried under undisturbed deposits allowing the effect of the structures on the currents to be assessed (Figure 1b). No excavations are permitted in these zones in order to protect the ruins from degradation. However, the Soprintendenza di Pompeii allowed new outcrops to be cleaned and sampled, offering a unique opportunity to examine the way in which the A.D. 79 PDCs interacted with the town.

## 2. A.D. 79 Deposits at Pompeii

[4] The A.D. 79 eruption of Vesuvius caused the total destruction of several Roman towns, including Pompeii, Stabiae, Oplontis and Herculaneum (Figure 1a) as well as isolated villas scattered around the flanks of the volcano, causing the death of more than 3,000 people [e.g., Lirer *et al.*, 1973, 1993; Sheridan *et al.*, 1981; Sigurdsson *et al.*, 1982, 1985; Carey and Sigurdsson, 1987; Cioni *et al.*, 1992, 2000, 2004]. Herculaneum, just 7 km west of Vesuvius, was destroyed and completely buried by dense PDCs [e.g., Sigurdsson *et al.*, 1985; Cioni *et al.*, 2000; Gurioli *et al.*, 2002]. Pompeii, 9 km southeast of Vesuvius, was first covered by 2.5 m of fall deposits and was then partially destroyed by a series of turbulent PDCs [e.g., Sigurdsson *et al.*, 1985; Cioni *et al.*, 2000; Luongo *et al.*, 2003a, 2003b; Gurioli *et al.*, 2005]. White and then gray pumice (EU2 and EU3, Figure 2) fell from a Plinian column that was sustained for 18 hours and reached elevations of up to 32 km [Carey and Sigurdsson, 1987; Macedonio *et al.*, 1988; Barberi *et al.*, 1990].

[5] During this Plinian phase, some minor PDCs were generated by the discontinuous collapse of marginal portions of the convective column. Only the last of these events reached the northwestern edge of Pompeii (EU3pfi, Figure 2a). This PDC left a 2- to 7-cm-thick ash layer at the edge of the town interbedded with, and topping the fallout deposit [Cioni *et al.*, 2000]. The town was covered by a 4- to 30-cm-thick ash layer (EU3pf, Figure 2) emplaced by a very dilute PDC, derived from the total collapse of the Plinian column [Cioni *et al.*, 2000]. This layer was then mantled by a 3- to 6-cm-thick fall deposit (EU4, Figure 2). EU4 was emplaced by a second, short-lived, lithic-rich column that persisted for just 25 min [Gurioli, 2000]. The collapse of this second column generated the most powerful and turbulent PDC,

EU4pf [Cioni *et al.*, 1992, 1996, 2004], which destroyed the town partially and emplaced relatively coarse-grained, meter-thick deposits (EU4pf, Figure 2). Finally, the settlement was buried by a 1 m thickness of very dilute PDCs and fall deposits (EU7 and EU8, Figure 2) consisting of ash and accretionary lapilli, emplaced during the final phreatomagmatic phase of the eruption. In this paper the focus is on the EU3pf and EU4pf deposits which display the greatest degree of interaction with the town. EU3pf and EU4pf interacted with many walls still protruding through the 2.5-m-thick fallout layer and impacted a town in which all roofs had already collapsed due to the weight of fall pumice [Macedonio *et al.*, 1988]. The EU7pf and EU8 deposits are also briefly described. These mantle the complex EU3pf-EU4pf stratigraphy but show no evidence of perturbation by the town.

## 3. Methods

[6] The approach focused on identifying all remaining outcrops within and around the town where instructive deposits occurred within buildings. Field-based analyses comprised mapping [Giannini *et al.*, 2000], logging and sampling of these known and newly discovered outcrops (Figure 1). Rock magnetic measurements were then made to quantify the PDC flow directions and deposit temperature,  $T_{\text{dep}}$  (as defined by Cioni *et al.* [2004]), as well as grain size analyses to reveal lateral and vertical variations in the parent current. Finally, integration of these data with sedimentological descriptions and measurements allowed a model to be constructed of the behavior of PDCs entering, and moving through, a town.

### 3.1. Magnetic Fabric

[7] Rock magnetism has manifold applications to the analysis of PDC deposits. Investigation of the thermal remanence (TRM) provides paleomagnetic information as well as constraint of the PDCs' deposit temperature [e.g., Bardot, 2000; Bardot and McClelland, 2000; Kent *et al.*, 1981; McClelland and Druitt, 1989; Cioni *et al.*, 2004]. The anisotropy of magnetic susceptibility (AMS) allows quantification of the magnetic fabric, which is then interpreted to yield the direction of the flow in the lower part of the current. This can give the direction of the flow, which can be used to obtain vent location and/or local flow dynamics [e.g., Hillhouse and Wells, 1991; Ort *et al.*, 1999, 2003; Palmer and MacDonald, 1999]. A combination of both TRM and AMS analyses gives the most complete information regarding flow direction and  $T_{\text{dep}}$  and is thus a powerful approach to a better understanding of PDC emplacement processes [Gurioli *et al.*, 2005]. Consequently this approach has been applied to the PDC deposits of the A.D. 79 eruption. Here, the focus is primarily on the AMS results to infer PDC flow directions and the effect of the urban fabric on these. A companion paper [Zanella *et al.*, 2007] deals with the  $T_{\text{dep}}$ .

**Figure 1.** Location map of the studied area. (a) Shaded relief map of the southern sector of the Vesuvius region. Isopachs (in cm) indicate the total thickness of the PDC deposits emplaced by the A.D. 79 eruption around and within Pompeii. Inset shows location of Vesuvius in Italy. (b) Ancient Roman town of Pompeii. The main street, Via dell'Abbondanza, has been highlighted. Dots indicate sites of studied sections and AMS sampling; yellow areas indicate portions of ruins still buried by undisturbed A.D. 79 deposits. Top right inset shows site 11, Casa dei Casti Amanti; bottom left inset shows site 12, rooms in Castricio area.

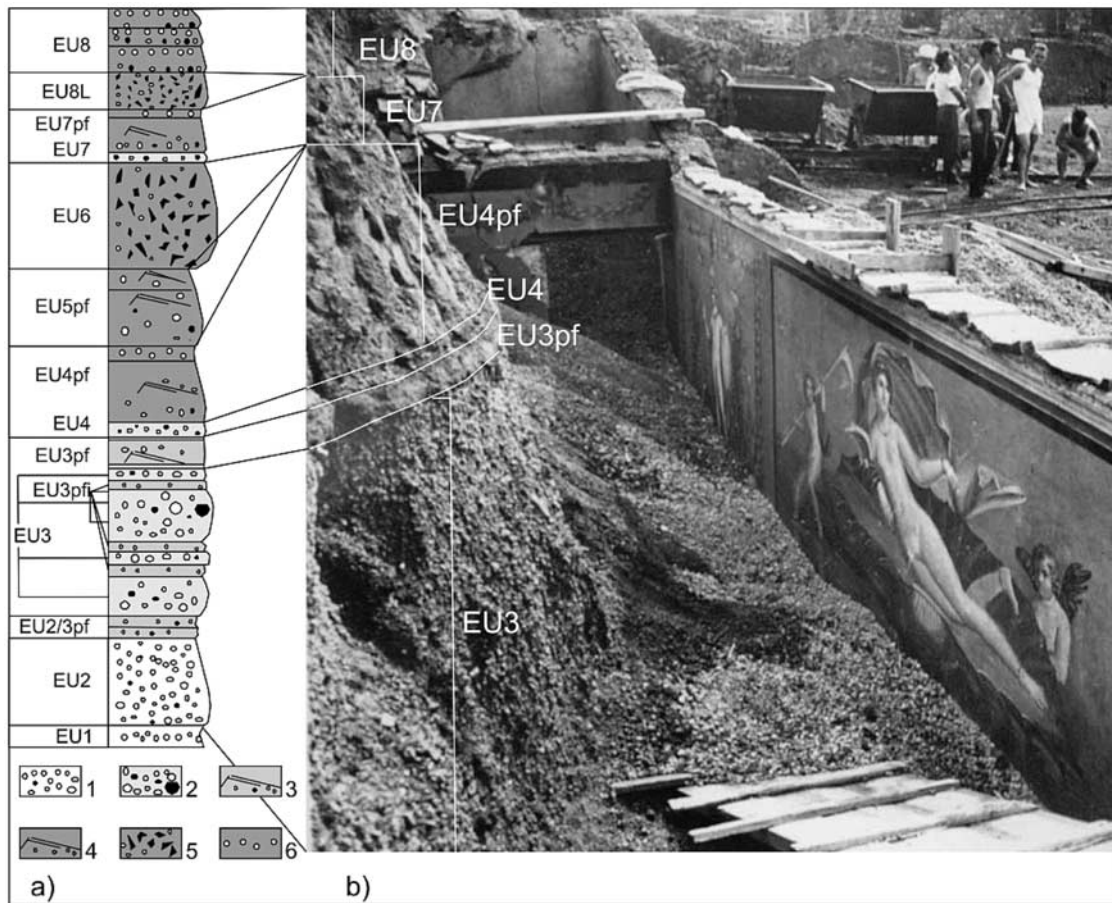


**Figure 2.** A.D. 79 deposits at Pompeii. (a) Schematic stratigraphy of the deposits of the A.D. 79 eruption, according to the nomenclature of *Cioni et al.* [1992, 2004]. Legend: 1, white pumice lapilli and bombs; 2, gray pumice lapilli and bombs; 3, magmatic, massive to stratified coarse-grained ash and gray pumice lapilli; 4, stratified coarse-grained ash, gray pumice and lithic lapilli; 5, lithic blocks and gray pumice lapilli in coarse ash matrix; 6, accretionary lapilli in coarse and fine ash matrix. (b) Complete sequence of the A.D. 79 pyroclastic deposits in the archaeological excavations at Casa della Venere (regio II, insula II, west Pompeii, courtesy Soprintendenza di Pompei).

### 3.1.1. AMS

[8] The magnetization acquired by a solid body under the influence of an external magnetic field varies according to the direction of the field relative to the body. Easy magnetization direction of individual grains of a rock are either related to their crystallographic axes (as for hematite) or to their shape (as for magnetite). In the latter case, the magnetization acquired by a grain of magnetite (multidomain or pseudosingle-domain) is higher when the applied field is parallel to the longest dimension of the grain and is lower when it is orthogonal. The AMS of a rock thus depends on its minerals and on the spatial arrangement of their grains. The fine-grained pyroclastic deposits of the A.D. 79 eruption contain low-Ti titanomagnetite as the main ferromagnetic mineral [Zanella et al., 2000; Gurioli et al., 2002]. The content of this mineral is high enough (mean bulk susceptibility 3000 to 6000  $\mu\text{SI}$  unit) to mask the contribution of paramagnetic and diamagnetic minerals. The magnetic fabric of the deposits therefore depends on the spatial arrangement of inequant (titano) magnetite grains. As magnetic susceptibility is represented by a

second-order, symmetric tensor, the AMS is described by a triaxial ellipsoid. The axes of this ellipsoid correspond to the principal susceptibility directions ( $k_{\text{max}} > k_{\text{int}} > k_{\text{min}}$ ) and the shape is defined by three parameters. These are: the degree of anisotropy,  $P = k_{\text{max}} / k_{\text{min}}$ , the magnetic lineation,  $L = k_{\text{max}} / k_{\text{int}}$ , and the magnetic foliation,  $F = k_{\text{int}} / k_{\text{min}}$  [Jelinek, 1977]. The magnetic fabric of pyroclastic density current deposits is usually well developed and can be related to flow direction due to the fact that elongated grains tend to align themselves parallel to the flow direction. A normal fabric is one in which the foliation plane (the plane orthogonal to the minimum axis,  $k_{\text{min}}$ ) is close to the horizontal ( $<20^\circ$ ) and imbricated upstream (Figure 3a) and the lineation (the direction corresponding to the maximum axis,  $k_{\text{max}}$ ) is imbricated in the same way. These characteristics allow identification of the flow direction. This interpretation of the magnetic fabric is also supported by traditional microfabric analysis of the phenocryst arrangement [e.g., Schmincke and Swanson, 1967; Elston and Smith, 1970; Suzuki and Ui, 1982; Ui et al., 1989], as well as by the alignment of macrofabric elements, such as

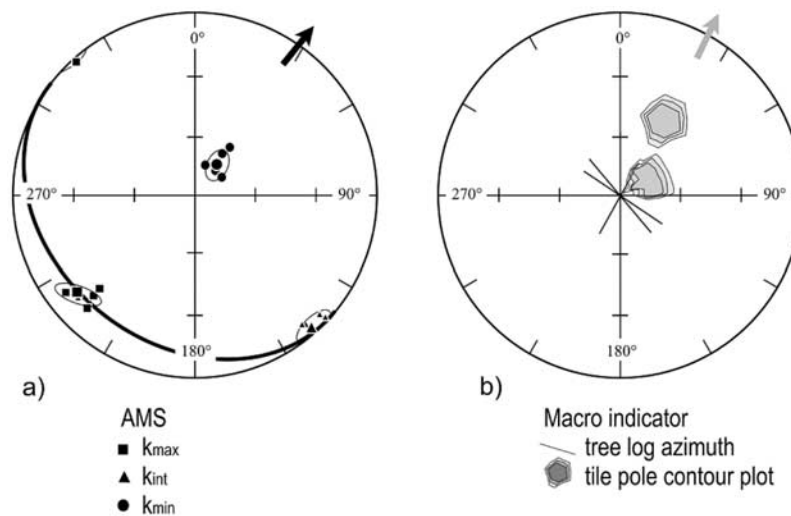


**Figure 3.** Microfabric and macrofabric indicators in the pyroclastic deposits at Pompeii. (a) Equal-area projection of the principal susceptibility axes and associated ellipses of confidence. Great circle indicates magnetic foliation; square indicates magnetic lineation; black arrow indicates inferred flow direction. (b) Equal-area projection of the contour plot of the tiles poles and azimuth of tree log remains. Tile pole indicates pole of the plan coinciding with the tile's largest flat dimension; gray arrow indicates inferred flow direction.

fiammae or elongated lithic clasts [e.g., Schmincke and Swanson, 1967; Kamata and Mimura, 1983; Hughes and Druitt, 1998]. In the case of Pompeii, a unconventional macrofabric element is provided by the tiles that fell to the ground during roof collapse during the first phase of the eruption. These were then picked up by the PDCs [Gurioli *et al.*, 2002]. Roman tiles were shaped like slabs with dimensions of up to  $40 \times 40 \times 2$  cm. Their presence is quite common in the PDC deposits, typically as broken fragments ranging from pieces just a few centimeters across to nearly unbroken tiles. Whenever present these tile fragments were sampled by orienting their flat side in the same way as used to orient paleomagnetic hand samples. Irrespective of their dimensions, the fragments were orientated so that they are flat lying and imbricated upstream with an orientation that coincides with the microfabric foliation given by AMS measurements (Figure 3b). Both the magnetic foliation and magnetic lineation can be used as a proxy for the flow direction [Hillhouse and Wells, 1991; MacDonald and Palmer, 1990], but the imbrication of the foliation plane is more reliable than the lineation. Lineation may be dispersed within the foliation plane and may even be orthogonal to the flow direction. The PDC fabric is usually foliated, so the AMS ellipsoid is strongly oblate. This can cause the  $k_{\max}$  and  $k_{\text{int}}$  directions to be dispersed along a girdle within the foliation plane, so that they are not well defined or even statistically undistinguishable. On the other hand, elongate grains may, rather than aligning themselves parallel to the flow, align themselves across it. This is the case for the orientation of two out of three tree logs (Figure 3b). This may occur when grains, carried by traction in the current, are rolled along the depositional surface [e.g., Smith, 1986; Bryan *et al.*, 1998] as also observed in turbidites [e.g., Ellwood and Ledbetter, 1977; Ledbetter and Ellwood, 1980]. When interpreting these results it has

been assumed that the flow direction is represented by the azimuth of the magnetic foliation pole, i.e., the site-mean azimuth (D) of  $k_{\min}$ .

### 3.1.2. Sampling

[9] The sampling included sites with different relationships to the main PDC flow direction and the orientation of the Roman ruins. These included undisturbed sites in open country around the city, sites along the city walls and the road network formed by the decumanus (oriented E–W) and the cardo (N–S) streets within the town, as well as sites inside a villa and other buildings. The deposits were extremely loose and coring in the field proved impossible. Therefore coherent blocks of material were removed from the deposit and returned to the laboratory where coring could be completed. This was achieved by identifying a suitable coherent section of the outcrop. The selected area was then cleaned and the orientation was measured with both magnetic and Sun compasses, and a clinometer. An orientation mark was next carved on the face and fixed with a triangle of pins. The block was then carefully carved out taking care not to disturb the block face. Blocks were typically 10 cm high, 20 cm wide and 20 cm deep. Removing the samples in this way was difficult and many were lost when they cracked or crumbled during carving or removal. Upon removal the block was tightly wrapped in multiple layers of cellophane to keep them intact during transport to the laboratory. In the laboratory they were bathed in ethyl-silicate for a couple of days and then left to harden on a wooden shelf for a couple of weeks. They were then cored in the laboratory to provide cylindrical specimens of standard analysis size (diameter 25.4 mm, height 22 mm). As the degree of hardening strongly depended on the sample's permeability, which was highly variable, the results of the coring process were not fully satisfactory. A total of 159 specimens were prepared from



**Table 1.** Site Mean AMS Data for the EU4pf Deposits of the Vesuvius A.D. 79 Eruption at Pompeii<sup>a</sup>

Site	Facies	n/N	Color	k <sub>m</sub> , μSI	L	F	P	Foliation Pole				Lineation				V
								D	I	Angles		D	I	Angles		
										Confidence	Ellipse			Confidence	Ellipse	
1b	M (top)	2/2	black	5320	1.006	1.011	1.017	176	68	14.4	2.7	44	15	13.1	12.1	51
1b	CB (base)	2/2														
2a	CB (middle/top)	6/6	black	5500	1.005	1.015	1.020	170	76	3.5	1.9	338	14	5.6	3.4	59
2b	M (base)	10/12	black	5130	1.004	1.007	1.011	149	74	11.7	6.4	333	16	16.5	10.7	55
8a	CB	6/6	black	4720	1.008	1.021	1.029	147	79	2.5	1.0	309	10	7.3	2.3	58
14 - top	CB (top)	6/6	black	3890	1.002	1.006	1.008	122	62	8.8	1.2	332	25	54.1	2.5	69
19	SCF (middle)	4/4	black	5213	1.009	1.007	1.016	136	64	24.7	13.9	17	13	28.4	13.2	37
19	CS (base)	2/2														
5e	SCF (base)	5/5	hollow	4170	1.005	1.010	1.015	39	73	6.5	4.7	230	17	8.3	3.1	58
6	M (middle)	6/6	hollow	4770	1.005	1.005	1.010	84	74	23.0	3.1	262	16	28.2	10.7	58
7a - high	SCF (top)	5/6	hollow	5285	1.005	1.011	1.016	113	78	13.7	11.3	322	11	48.8	13.6	67
7a - high	SCF (middle)	5/5														
7a - high	M (base)	5/5														
10	PP (top)	2/2	hollow	5200	1.01	1.011	1.021	114	81	18.4	4.3	305	9	19	3.9	50
10	CB (middle)	2/2														
12c	M (base)	6/6	hollow	5970	1.008	1.014	1.022	142	79	11.6	5.1	330	11	8.1	3.6	54
24	SCF	5/5	hollow	5130	1.008	1.014	1.022	80	65	30.6	5.5	331	9	24.2	7.7	47
7a - low	SCF (top)	3/3	blue	4650	1.004	1.008	1.012	190	78	16.6	10	280	0	61.6	15.4	71
7a - low	SCF (middle)	5/5														
7a - low	M (base)	4/4														
7b	M (base)	9/10	blue	4600	1.004	1.008	1.012	153	74	25.0	17.6	285	11	40.2	14.4	52
14 - base	M (base)	5/5	blue	4785	1.008	1.025	1.034	195	80	12.2	1.3	300	3	10.3	7.2	59
25	ULB	13/13	blue	4370	1.003	1.007	1.010	202	75	15.8	7.9	8	15	22.7	14.3	54
2c	M (base)	11/12	orange	4780	1.003	1.009	1.012	2	79	8.3	7.5	141	8	51.3	7.8	63
11f	ULB (middle)	6/6	orange	4420	1.005	1.010	1.015	259	75	11.6	1.0	152	5	45.6	1.0	60
11g	ULB (middle)	5/5	orange	3960	1.005	1.012	1.017	52	64	11.4	2.4	159	8	26.3	4.5	63
12a	ULB (middle)	2/2	orange	5500	1.007	1.011	1.018	302	67	26	8.2	115	23	22.9	10.2	52
12a	M (base)	3/3														
12b	M (base)	6/6	orange	3370	1.002	1.003	1.005	350	51	55.7	7.2	250	8	22.5	7.1	46
21	CB (top)	1/1	orange	5065	1.005	1.006	1.011	11	74	26.7	15.5	119	5	71.8	15	69

<sup>a</sup>Symbols are N, total number of specimens; n, number of measured cores; color, color of the arrows in Figure 6;  $k_m$ , bulk susceptibility; L, magnetic lineation; F, magnetic foliation; P, degree of anisotropy; foliation pole: D, I, declination, inclination of the  $k_{\min}$  axis with radii of the confidence ellipse (E3-2, E3-1); lineation: D, I, declination, inclination of the  $k_{\max}$  axis with radii of the confidence ellipse (E1-2, E1-3). Nomenclature of the facies is as in Figure 5.

66 samples collected at 23 sites, from unit EU4b. Four samples were also collected from EU3pf and EU7pf, but these were insufficient for statistical analysis.

### 3.1.3. Measurements

[10] All measurements were carried out at the ALP laboratory (Peveragno, Italy) using AGICO bridges KLY 2 and KLY 3. The principal directions proved to be well defined at the specimen level and their site mean values were computed using Jelinek's statistics [Jelinek, 1977]. Bulk susceptibility and anisotropy parameters were calculated as

arithmetic means (Table 1). The degree of anisotropy, P, was very low, in all cases being higher than 1.02 at only six sites and with a maximum value of 1.034. The magnetic fabric was, however, well defined and two main types of geometry were recognized. In the first type (Figure 4a) all three principal directions were tightly grouped and both magnetic foliation and lineation were well defined. In the second type (Figure 4b) the  $k_{\min}$  axes were well grouped, but the  $k_{\max}$  and  $k_{\text{int}}$  axes were dispersed along a girdle. Magnetic foliation was therefore better defined than lineation.

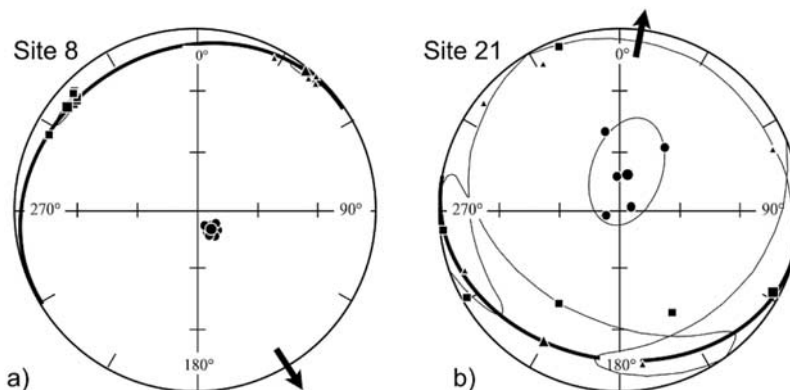


**Figure 4.** Type of magnetic fabric in the pyroclastic deposits at Pompeii (same symbols as in Figure 3).

Table 2. Grain Size and Facies Data Analyses of EU3pf Deposits<sup>a</sup>

Site and Section	Bed <sub>c</sub> , cm	Sample	Facies <sub>c</sub> , cm	L <sub>c</sub> , cm	H <sub>c</sub> , cm	MP, cm	ML <sub>c</sub> , cm	MB <sub>c</sub> , cm	$\phi_5$ , $\phi$	$\phi_{16}$ , $\phi$	$\phi_{25}$ , $\phi$	$\phi_{75}$ , $\phi$	$\phi_{84}$ , $\phi$	$\phi_{95}$ , $\phi$	Mz <sub>c</sub> , $\phi$	Md $\phi$ , $\phi$	$\sigma\phi$ , $\phi$	F1, %	F2, %	L <sub>c</sub> , %	CA, %
Antonio (1a)	5_16	P15	4_9	10	2	1.4	3.0	Nord	-1.27	-0.06	0.56	3.71	4.03	4.15	2.02	2.07	2.05	83	21	4	75
Antonio (1a)	5_16		0_2																		
Antonio (1a)	5_16		1_5																		
Antonio (1b)	5_17		0_10			1.4	3.0														
Antonio (1b)	5_17		0_2																		
Antonio (1b)	5_17		5_																		
Villa Misteri (2a)	7_13		1																		
Villa Misteri (2a)	7_13	P80	2_7		2	1.0	0.5		-1.41	0.17	0.85	3.82	4.04	4.15	2.18	2.33	1.94	86	22	5	73
Villa Misteri (2a)	7_13		0_2																		
Villa Misteri (2a)	7_13		2_3																		
Villa Misteri (2b)	7_25		1																		
Villa Misteri (2b)	7_25	P12	1_17		2	1.8	3.0		-2.12	-0.79	0.12	4.01	4.06	4.16	1.80	2.12	2.42	75	26	10	64
Villa Misteri (2b)	7_25		1_2																		
Villa Misteri (2b)	7_25		4_5																		
Villa Misteri (2c)	7_24		1																		
Villa Misteri (2c)	7_24	P87	3_20		2.0	2.0	1.5		-3.52	-2.53	-1.82	3.49	4.02	4.14	0.68	0.55	3.28	54	20	29	52
Villa Misteri (2c)	7_24		3_																		
Via delle Tombe (23)	7_5		1.5																		
Via delle Tombe (23)	7_5		3		1.5	0.5	0.5														
Via delle Tombe (23)	7_5		0.5																		
Via delle Tombe (23)	7_5		2.5																		
Villa Diomede (3)	8_9		2																		
Villa Diomede (3)	8_9		4		1	2.0	2.0														
Villa Diomede (3)	8_9		0_1																		
Villa Diomede (3)	8_9		2																		
Porta Ercolano (4)	7_		1																		
Porta Ercolano (4)	7_		3		2	0.5	0.5														
Porta Ercolano (4)	7_		1																		
Porta Ercolano (4)	7_		2																		
Porta Ercolano (4)	6_8		1																		
P.Ere-P.Ves (5a)	6_8		3			1.0	0.5														
P.Ere-P.Ves (5a)	6_8		1_2																		
P.Ere-P.Ves (5a)	6_8		1_2																		
P.Ere-P.Ves (5d)	6_		1																		
P.Ere-P.Ves (5d)	6_		2.5			1.0	0.5														
P.Ere-P.Ves (5d)	6_		0.5																		
P.Ere-P.Ves (5d)	6_		2																		
P.Ere-P.Ves (5e)	7_5_14_5		1.5																		
P.Ere-P.Ves (5e)	7_5_14_5		2.8		2	1.6	0.5	2 (tiles)													
P.Ere-P.Ves (5e)	7_5_14_5		1_2																		
P.Ere-P.Ves (5e)	7_5_14_5		3_																		
P.Ere-P.Ves (5e)	4_4_		0.4																		
P.Ere-P.Ves (5g)	4_4_		1.5																		
P.Ere-P.Ves (5g)	4_4_		0.5																		
P.Ere-P.Ves (5g)	4_4_		2																		
Porta Capua (6)	6_15		1																		
Porta Capua (6)	6_15	P18	3_9		0.5	1.4	2.5		-1.05	-0.13	0.44	3.42	3.92	4.11	1.88	1.85	2.03	71	25	18	58
Porta Capua (6)	6_15		0_1																		
Porta Capua (6)	6_15		2_4																		



Table 2. (continued)

Table 2. (continued)

Site and Section	Bed, cm	Sample	Facies <sub>t</sub> , cm	Facies	L <sub>c</sub> , cm	H <sub>c</sub> , cm	MP <sub>c</sub> , cm	ML <sub>c</sub> , cm	MB <sub>c</sub> , cm	$\phi_5$ , $\phi$	$\phi_{16}$ , $\phi$	$\phi_{25}$ , $\phi$	$\phi_{75}$ , $\phi$	$\phi_{84}$ , $\phi$	$\phi_{95}$ , $\phi$	Mz <sub>c</sub> , $\phi$	Md $\phi$ , $\phi$	$\sigma\phi$ , $\phi$	F1, %	F2, %	L, %	CA, %
Casa Casti Amanti (11g)	6_18	P67	0_3	IIJFP						-2.75	-1.92	-1.52	1.60	3.31	4.10	0.28	-0.55	2.61	40	12	26	62
Casa Casti Amanti (11g)	6_18		4_	IJM																		
Castricio (12ahigh)	5_	P39	2.5	IIJCS						-4.01	-2.06	-1.04	4.01	4.06	4.17	1.23	1.70	3.06	63	27	21	52
Castricio (12ahigh)	5_		0.5	IIJFP																		
Castricio (12ahigh)	5_	P36	2	DM						-3.55	-2.73	-1.86	3.50	4.03	4.14	0.71	0.82	3.38	55	20	30	50
Castricio (12alow)	19	P38	11.5	IIJCS						-0.44	0.77	1.38	4.03	4.08	4.18	2.59	2.92	1.65	92	31	2	67
Castricio (12alow)	19	P37	3	IIJFP						-0.63	0.20	0.67	2.96	3.58	4.08	1.83	1.72	1.69	87	11	1	89
Castricio (12alow)	19	P35	2	IJM						-2.52	-1.51	-0.88	3.93	4.05	4.16	1.37	1.58	2.78	64	24	17	59
Castricio (12alow)	19	P34	2.5	IJFP						-3.55	-2.68	-1.89	3.08	3.87	4.11	0.77	1.11	3.27	57	15	30	56
Castricio (12c)	6_15	P52	3_7	IIJCS						-1.50	-0.23	0.38	3.76	4.04	4.15	1.92	1.96	2.13	81	22	5	73
Castricio (12c)	6_15	P51	1_4	IIJFP						-2.67	-1.94	-1.57	1.46	2.73	4.03	0.07	-0.57	2.33	39	8	27	65
Castricio (12c)	6_15		2_4	IJM																		
San Paolino (13)	4_7		2_3	IIJCS		1	0.8	1.4														
San Paolino (13)	4_7		0_1	IIJFP																		
San Paolino (13)	4_7		2_3	DM																		
Via dell'Abbondanza (24)	5_		2	IIJCS		0.5	1	1														
Via dell'Abbondanza (24)	5_		1	IIJFP																		
Via dell'Abbondanza (24)	5_		2	IJM																		
Vigneto (14)	5_		2	IIJCS		0.5	1	1.4														
Vigneto (14)	5_		1	IIJFP																		
Vigneto (14)	5_		2	DM																		
<i>Sud</i>																						
OldPortaMarina (20)	0	eroded																				
Scarp lava (25a)	7		2	IIJCS			0.8	0.8														
Scarp lava (25a)	7		2	IIJFP	80	2																
Scarp lava (25a)	7		3	DM																		
Scarp lava (25b)	5		2	IIJCS			0.5	0.5														
Scarp lava (25b)	5		0	IIJFP																		
Scarp lava (25b)	5		3	IJM																		
Stabia (21)	4_5	P5	2	IIJCS		0.5	2.6	1.8		-0.89	-0.19	0.29	3.50	4.03	4.14	1.78	1.49	2.11	80	20	1	79
Stabia (21)	4_5		0_1	IIJFP																		
Stabia (21)	4_5		2	DM																		
Necropolis (22c)	6_20	P43	3_14	IIJULB	25	6	2	2.6		-3.23	-2.17	-1.52	3.36	4.00	4.12	0.82	0.63	3.09	56	16	25	59
Necropolis (22c)	6_20		0_3	IIJFP																		
Necropolis (22c)	6_20		3	IJM																		
Necropolis (22b)	5	Po-40	2	IIJCS			0.8	0.5		-2.59	-1.01	-0.25	3.53	4.02	4.14	1.58	1.72	2.52	72	19	12	68
Necropolis (22b)	5	Po-39	1	IIJFP		1				-0.63	0.30	0.73	3.09	3.60	4.08	1.91	1.84	1.65	89	11	1	88
Necropolis (22b)	5	Po-38	2	DM						-4.00	-2.14	-1.23	2.80	3.66	4.10	0.77	0.78	2.90	59	13	22	65
Necropolis (22d)	4		1.5	IIJCS		0.5	0.8	0.5														
Necropolis (22d)	4		0.5	IIJFP																		
Necropolis (22d)	4		2	IJM																		
Necropolis (22a)	5		2	IIJCS		0.5	0.8	0.8														
Necropolis (22a)	5		1	IIJFP																		
Necropolis (22a)	5		2	DM																		
lozzino (26)	5_17.5		3_14	IIJCS																		
lozzino (26)	5_17.5		0.5_2	IIJFP																		
lozzino (26)	5_17.5		1.5_	IJM																		

Table 2. (continued)

Site and Section	Bed, cm	Sample	Facies, cm	Facies	L, cm	H, cm	MP, cm	ML, cm	MB, cm	$\phi 5$ , $\phi$	$\phi 16$ , $\phi$	$\phi 25$ , $\phi$	$\phi 75$ , $\phi$	$\phi 84$ , $\phi$	$\phi 95$ , $\phi$	Mz, $\phi$	Md $\phi$ , $\phi$	$\sigma\phi$ , $\phi$	F1, %	F2, %	L, %	CA, %
Scarp_ViaFarnacista (16)	6		3	IDCS		0.5	1	1														
Scarp_ViaFarnacista (16)	6		1	IDFP																		
Scarp_ViaFarnacista (16)	6		2	DM																		
Outside_ViaFarnacista (17)	6		2	IDCS		0.5	0.7	1														
Outside_ViaFarnacista (17)	6		1	IDFP																		
Outside_ViaFarnacista (17)	6		3	DM																		
Outside_soprastanti (18)	6.24		3.18	IDCS		2	2.5	4	6 (mortars)													
Outside_soprastanti (18)	6.24		1.2	IDFP																		
Outside_soprastanti (18)	6.24		2.4	DM																		
Scarp_Soprintendenza (19)	5.7.5		2.3	IDCS		0.5	0.8	2														
Scarp_Soprintendenza (19)	5.7.5		0.5.2	IDFP																		
Scarp_Soprintendenza (19)	5.7.5		1.2.5	DM																		

<sup>a</sup>Bed, bed thickness variation; sample, collected sample; Facies, facies thickness variation; facies, facies of each single subunits (nomenclature as in Figure 5); L, length of dune or lenses; H, height of dune or lenses; MP, maximum pumice diameter; LM, maximum lithic diameter; MB, maximum debris diameters (tiles, piece of wall, logs eroded by the PDC);  $\phi 5$  up to  $\phi 95$ , percentile; Mz, mean diameter [from *Folk and Ward*, 1957]; Md $\phi$ , mean diameter;  $\sigma\phi$ , sorting [from *Imman*, 1952]; F1, weight percentage of fractions finer than 1 mm; F2, weight percentage of fractions finer than 1/16 mm; L, weight percentage of lapilli; CA, weight percentage of coarse ash.

tion, whose statistical definition was poor in cases where the ellipses of confidence for  $k_{\max}$  and  $k_{\text{int}}$  intersected.

### 3.2. Nomenclature and Field-Based Analysis

[11] Several pyroclastic facies have been identified in each flow unit of the A.D. 79 eruption. These have been related to different emplacement mechanisms, as previously presented for the A.D. 79 PDC deposits cropping out in Herculaneum by *Gurioli et al.* [2002]. The PDCs can be described as stratified currents divided into two parts. Following *Britter and Hanna* [2003], the lower part of the current was defined as the layer that is directly affected by the local obstacles, the upper part as the layer unaffected by the underlying urban surface. For simplicity, the upper part also includes a medial-transitional zone in which the current is still adjusting to the effects of the obstacles, but within which the effects are not as severe as at the base [see *Britter and Hanna*, 2003, Figure 2]. The internal stratification of a turbulent density current is, in reality, much more complex [e.g., *Dellino and La Volpe*, 2000], but, for simplicity, this simple twofold division was used. It is the lower part of this division, that which interacted with the urban fabric, in which there is most interested.

[12] Thickness, grain size, fabric, grading, and stratification (wavelength and amplitude of dunes as well as length and height of lenses and layers) of the deposits were examined. These were measured for each pyroclastic unit cropping out inside or around the excavated area, where the measurements for each section are given in Tables 2, 3, and 4. The average size of the five largest clasts (pumice and nonjuvenile lithics, respectively, MP and ML) was measured for each unit. This was achieved by taking the mean of the three orthogonal lengths for each clast. The clasts were taken from the first (lowermost) normally graded, massive portion of the PDC deposits, whose sedimentary features were indicative of deposition directly from the turbulent suspension. The sedimentological nomenclature used in the classification of bed thickness, grain size and sorting follows that of *Sohn and Chough* [1989] and is summarized in Table 5. The interpretation of the facies follows *Sohn and Chough* [1989], *Chough and Sohn* [1990], and *Gurioli et al.* [2002]. As part of this, the lateral facies variations and vertical facies associations were defined for each flow unit and their distribution was used to place constraints both on transport and depositional processes and, most importantly, to emphasize the variations caused by the interactions with the urban fabric. Stratigraphic correlation of the different pyroclastic flow units out cropping at Pompeii permits eight main facies to be distinguished based on the sedimentary structures of the deposits (Figure 5). Grain size analyses were performed, following the procedure proposed by *Barberi et al.* [1989], on 100 samples from different sites and stratigraphic positions. To assess vertical variations in grain size, the depositional units were subdivided into several intervals. All the analyzed samples show a high content of coarse ash and a variable content of fine ash, which never exceeds 40% (Figures 5a and 5c). The coarsest grained samples were represented mainly by some facies of EU4pf (Figures 5a and 5b).

Table 3. Grain Size and Facies Data Analyses of EU4pf Deposits<sup>a</sup>

Site and Section	Bed <sub>0</sub> cm	Sample	Facies <sub>0</sub> cm	Facies	L, cm	H, cm	MP, cm	ML, cm	MB, cm	$\phi_5$ , $\phi$	$\phi_{16}$ , $\phi$	$\phi_{25}$ , $\phi$	$\phi_{75}$ , $\phi$	$\phi_{84}$ , $\phi$	$\phi_{95}$ , $\phi$	Mz, $\phi$	Md $\phi$ , $\phi$	$\sigma\phi$ , $\phi$	F1, %	F2, %	L, %	CA, %
<i>Nord</i>																						
Antonio (1a)	37_49		13_15	c)AL																		
Antonio (1a)	37_49		8_9	b)M																		
Antonio (1a)	37_49	P17	10_15	b)M			1.0	3.0		-0.90	0.26	0.85	3.58	4.01	4.13	2.15	2.16	1.88	87	18	2	80
Antonio (1a)	37_49	P16	6_10	b)CB	45	3				-0.80	0.37	1.02	3.94	4.05	4.16	2.30	2.49	1.84	89	24	2	74
Antonio (1b)	90		10	c)AL																		
Antonio (1b)	90		15	b)CB																		
Antonio (1b)	90		50	b)M			1.0	3.0														
Antonio (1b)	90		15	b)CB																		
Villa Misteri (2a)	100_215		11	c)AL																		
Villa Misteri (2a)	100_215	P85	0_12	b)CB						-0.81	0.60	1.22	4.01	4.06	4.17	2.44	2.66	1.73	89	28	3	69
Villa Misteri (2a)	100_215	P84	10_18	b)CB						-1.63	0.36	1.35	4.00	4.05	4.16	2.40	2.79	1.85	86	25	5	70
Villa Misteri (2a)	100_215	P83	0_55	b)CB	320	55				-1.14	0.08	0.76	3.45	3.90	4.11	2.05	2.16	1.91	85	14	3	83
Villa Misteri (2a)	100_215	P82	35_43	b)ULB					30 (logs)	-1.24	0.38	1.30	4.01	4.06	4.17	2.44	2.88	1.84	87	28	4	68
Villa Misteri (2a)	100_215	P81	55_76	b)M			2.3	4.4	15 (tiles)	-3.46	-2.93	-2.59	2.73	3.71	4.10	-0.16	-1.27	3.32	42	13	48	39
Villa Misteri (2b)	360		10	c)AL																		
Villa Misteri (2b)	360		150	b)CB	300	100																
Villa Misteri (2b)	360	P13	200	b)M			3.0	10.0		-3.80	-3.23	-2.87	2.92	4.00	4.12	-0.05	-0.92	3.61	44	16	45	39
Villa Misteri (2c)	110_159		13_16	c)AL																		
Villa Misteri (2c)	110_159	P9	20_43	b)ULB	100	10				-1.47	-0.22	0.80	4.05	4.10	4.20	2.37	3.23	2.16	82	38	5	57
Villa Misteri (2c)	110_159	P8	77_100	b)M			2.4	9.9	40 (tiles)	-3.61	-3.09	-2.67	3.46	4.02	4.13	-0.14	-1.34	3.55	45	20	47	33
Via delle Tombe (23)	110		10	c)AL																		
Via delle Tombe (23)	110		7	b)CB																		
Via delle Tombe (23)	110		13	b)CB																		
Via delle Tombe (23)	110		63	b)CB																		
Via delle Tombe (23)	110		20	b)CS																		
Via delle Tombe (23)	110		17	b)M			1.0	1.0														
Via delle Tombe (23)	75		20	c)AL																		
Villa Diomede (3)	75		15	b)PP																		
Villa Diomede (3)	75		40	b)M			1.0	1.0														
Villa Diomede (3)	75		17	c)AL																		
Porta Ercolano (4)	139		4	b)PP																		
Porta Ercolano (4)	139		40	b)M																		
Porta Ercolano (4)	139		65	b)CB																		
Porta Ercolano (4)	139		13	b)M			1.0	1.0	5 (tiles)													
Porta Erc-Pves (5a)	113	P24	13	c)AL					110 (logs)	-3.02	-1.40	-0.66	4.04	4.09	4.19	1.58	2.04	2.74	65	34	15	52
Porta Erc-Pves (5a)	113		85	b)SCF																		
Porta Erc-Pves (5a)	113	P23	15	b)SCF	10	10	5.0	6.0	16 (tiles)	-2.28	-0.75	0.25	3.93	4.05	4.16	1.89	2.36	2.40	77	24	10	66
Porta Erc-Pves (5d)	56		10	c)AL																		
Porta Erc-Pves (5d)	56		36	b)SCF			2.0	2.0														
Porta Erc-Pves (5d)	56		10	b)SCF	5	5																
Porta Erc-Pves (5e)	110		20	c)AL																		
Porta Erc-Pves (5e)	110		80	b)SCF																		
Porta Erc-Pves (5e)	110	P22	10	b)SCF	10	10	1.0	1.0		-2.53	-0.63	1.13	4.02	4.07	4.17	2.16	3.03	2.35	81	29	11	60
Porta Erc-Pves (5g)	193		128	b)SCF																		
Porta Erc-Pves (5g)	193	P20	65	b)ULB	10	10	3.0	3.0	5 (tiles)	-3.97	-3.19	-2.78	0.66	2.09	3.14	-0.90	-1.59	2.64	29	1	52	48
Porta Capua (6)	55_70		15	c)AL																		
Porta Capua (6)	55_70		10_13	b)SCF	10	10																
Porta Capua (6)	55_70	P19	20_27	b)M			1.3	1.7	33 (logs)	-3.15	-1.69	-0.56	4.00	4.05	4.16	1.60	2.43	2.87	71	25	18	58
Porta Capua (6)	55_70		10_15	b)ULB	100	3	2.0		11 (tiles)													



Table 3. (continued)

Site and Section	Bed., cm	Sample	Facies, cm	Facies	L, cm	H, cm	MP, cm	ML, cm	MB, cm	$\phi_5$ , $^\circ$	$\phi_{16}$ , $^\circ$	$\phi_{25}$ , $^\circ$	$\phi_{75}$ , $^\circ$	$\phi_{84}$ , $^\circ$	$\phi_{95}$ , $^\circ$	Mz, $^\circ$	Md $\phi$ , $^\circ$	$\sigma\phi$ , $^\circ$	F1, %	F2, %	L, %	CA, %
Porta Nola (7a)low	250		15	c)AL																		
Porta Nola (7a)low	250	P30c	110	b)SCF						-1.55	0.02	0.87	3.89	4.05	4.15	2.16	2.40	2.02	84	23	5	71
Porta Nola (7a)low	250	P30b	110	b)SCF		100	10			-2.25	-0.09	1.38	4.04	4.09	4.19	2.37	3.11	2.09	83	34	10	57
Porta Nola (7a)low	250	P30a	15	b)M				1.9	9.0	-4.05	-3.23	-1.75	3.99	4.05	4.16	0.78	1.53	3.64	60	25	26	49
Porta Nola (7a)high	104		14	c)AL																		
Porta Nola (7a)high	104	P27c	40	b)SCF						-0.82	0.86	1.57	4.03	4.08	4.18	2.65	3.00	1.61	91	33	3	64
Porta Nola (7a)high	104	P27b	40	b)SCF						-0.78	0.51	1.30	4.01	4.07	4.17	2.45	2.78	1.78	89	28	2	70
Porta Nola (7a)high	104	P27a	10	b)M			2.0	1.1		-2.07	-1.05	-0.47	4.02	4.07	4.17	1.75	2.23	2.56	68	29	10	61
Porta Nola (7b)	92		82	b)CS																		
Porta Nola (7b)	92		10	b)M																		
Porta Nola (7b)	153		10	c)AL																		
Samo Street (9)	153		13	c)AL + M																		
Samo Street (9)	153		110	b)ULB		200	2	1.7	5.0													
Samo Street (9)	153		20	b)M																		
SE_SamoStreet (8a)	14_41		9_14	c)AL																		
SE_SamoStreet (8a)	14_41		5_27	b)CB		600	23	1.1	1.3													
SE_SamoStreet (8b)	19_76		17_20	c)AL																		
SE_SamoStreet (8b)	19_76		0_26	b)CB		165	11															
SE_SamoStreet (8b)	19_76		2_30	b)M		36	2	1.0	1.0													
SE_SamoStreet (8c)	62_142		10	c)AL																		
SE_SamoStreet (8c)	62_142		10	c)AL + M																		
SE_SamoStreet (8c)	62_142		15	b)M			2.0	1.0														
SE_SamoStreet (8c)	62_142	P95	6	b)SCF																		
SE_SamoStreet (8c)	62_142		17_95	b)M			1.4	1.9		-1.11	0.53	1.27	4.03	4.08	4.18	2.51	2.92	1.78	89	31	4	66
SE_SamoStreet (8c)	62_142		3_6	b)SCF																		
Town																						
Via Vesuvio (10)	100_165		12_15	c)AL																		
Via Vesuvio (10)	100_165	P48	40	b)PP																		
Via Vesuvio (10)	100_165	P47	40-80	b)CB		100	4			-1.12	0.25	0.98	3.66	4.02	4.14	2.23	2.40	1.88	87	19	4	77
Via Vesuvio (10)	100_165	P46	8_30	b)CS				1.9	1.9	-3.00	-1.09	0.09	3.52	4.02	4.13	1.66	2.05	2.56	77	19	14	67
Casti Amanti (11a)	70_180		12	c)AL						-5.02	-3.86	-3.46	2.10	3.40	4.09	-0.80	-1.93	3.63	33	12	55	33
Casti Amanti (11a)	70_180		5_10	c)AL + CB																		
Casti Amanti (11a)	70_180	P59	10	b)CB		150	10			-1.43	0.38	1.15	4.03	4.08	4.18	2.43	2.82	1.85	88	32	5	64
Casti Amanti (11a)	70_180	P58	10_18	b)CB						-0.52	0.96	1.56	3.91	4.04	4.15	2.59	2.78	1.54	92	23	2	75
Casti Amanti (11a)	70_180	P57	40_100	b)CB		1200	100			-2.47	-1.83	-1.45	2.39	3.38	4.08	0.44	-0.22	2.61	47	11	24	66
Casti Amanti (11a)	70_180		10_38	b)CB				1.7	8.9													
Casti Amanti (11d)	43		15	c)AL																		
Casti Amanti (11d)	43	P63	7	b)M						-2.19	-0.54	0.55	4.01	4.06	4.17	1.97	2.40	2.30	80	27	9	65
Casti Amanti (11d)	43	P62	21	b)CB		70	10	1.0	1.0	-3.02	-1.69	-0.70	3.90	4.04	4.15	1.55	2.29	2.87	68	23	18	59
Casti Amanti (11e)	40	P73	14	b)M						-0.91	0.63	1.54	4.05	4.10	4.20	2.69	3.33	1.74	89	38	3	59
Casti Amanti (11e)	40	P72	16	b)SCF				1.6	1.6	-3.02	-1.45	-0.06	4.01	4.06	4.17	1.80	2.77	2.76	75	27	16	57
Casti Amanti (11e)	40	P71bis	10	b)M						-1.77	-0.32	0.85	3.91	4.04	4.15	2.16	2.75	2.18	81	23	7	70
Casti Amanti (11e)	40	P74	40	b)CS			2.0	2.0		-3.39	-2.54	-1.72	4.01	4.06	4.17	1.05	1.64	3.30	59	27	27	46
Casti Amanti (11e)	65	P66c	41	b)M						-0.51	1.66	2.32	4.03	4.08	4.18	3.05	3.39	1.21	93	32	3	65
Casti Amanti (11f)	65	P66b	16	b)ULB		40	3	2.0	2.0	-1.60	0.28	1.25	3.98	4.05	4.16	2.36	2.76	1.88	86	25	5	70
Casti Amanti (11f)	65	P66a	8	b)CS						-3.58	-1.50	0.23	4.01	4.04	4.11	1.77	2.78	2.77	76	27	16	57
Casti Amanti (11g)	90	P71	20	b)M						-1.54	1.49	2.39	4.06	4.11	4.20	3.08	3.66	1.31	91	41	5	54
Casti Amanti (11g)	90	P70	30	b)ULB		60	10	2.0	2.0	-3.08	-1.73	-0.72	3.51	4.01	4.13	1.41	1.96	2.87	69	17	18	65
Casti Amanti (11g)	90	P69	40	b)CS						-4.05	-3.40	-2.81	2.60	3.57	4.10	-0.12	-0.52	3.48	45	12	40	48

Table 3. (continued)

Site and Section	Bed., cm	Sample	Facies, cm	Facies	L, cm	H, cm	MP, cm	ML, cm	MB, cm	$\phi_5$ , $^\circ$	$\phi_{16}$ , $^\circ$	$\phi_{25}$ , $^\circ$	$\phi_{75}$ , $^\circ$	$\phi_{84}$ , $^\circ$	$\phi_{95}$ , $^\circ$	Mz, $^\circ$	Md $\phi$ , $^\circ$	$\sigma\phi$ , $^\circ$	F1, %	F2, %	L, %	CA, %
Via Castricio (12a)high	120		30	c)AL + CS																		
Via Castricio (12a)high	120		60	b)ULB					220 (logs)													
Via Castricio (12a)high	120		30	b)CS			1.4	1.4	10 (tiles)													
Via Castricio (12a)low	170		30	c)AL																		
Via Castricio (12a)low	170	P42	120	b)ULB	120	20				-0.35	1.05	1.61	4.00	4.03	4.11	2.65	2.86	1.50	93	25	2	73
Via Castricio (12a)low	170	P41		b)ULB					70 (wall)	-0.98	0.88	1.84	4.02	4.07	4.17	2.72	3.19	1.60	89	30	3	68
Via Castricio (12a)low	170	P40	20	b)CS			1.4	1.4	10 (tiles)	-2.88	-1.80	-1.37	3.56	4.02	4.14	0.94	0.65	2.94	55	20	23	58
Via Castricio (12a)low	110_160		30	c)AL																		
Via Castricio (12b)	110_160		80_130	b)M			1.4	1.4														
Via Castricio (12c)	80_95		10	c)AL																		
Via Castricio (12c)	80_95		7_10	c)AL + M																		
Via Castricio (12c)	80_95	P55	40_50	b)CB	120	5				-0.98	0.36	1.26	3.97	4.05	4.16	2.40	2.78	1.84	87	25	3	73
Via Castricio (12c)	80_95		10	b)PP																		
Via Castricio (12c)	80_95	P54	10_15	b)M			1.5	2.0	10 (tiles)	-3.19	-1.99	-1.22	3.66	4.03	4.14	1.24	1.68	3.01	62	20	22	58
Via Castricio (12c)	80_95		10_25	c)AL					(bodies)													
San Paolino (13)	49_86		30_50	b)CB	120	10			200 (logs)													
San Paolino (13)	49_86		9	b)PP			1.9	9.8	10 (tiles)													
San Paolino (13)	49_86		1_10	c)AL																		
Via dell'Abbondanza (24)	8_32		7_22	b)SCF			0.5	0.5														
Vigneto (14)	80_95	P79	20	c)AL						-2.94	-2.22	-1.49	2.78	3.80	4.11		0.51	3.01	54	14	25	61
Vigneto (14)	80_95	P78	40_50	b)CB	125	10				0.08	1.35	1.93	4.02	4.07	4.18	2.84	3.11	1.36	96	30	1	69
Vigneto (14)	80_95	P77	10	b)PP			1.8	1.6		0.73	1.71	2.23	4.02	4.07	4.18	3.00	3.21	1.18	98	30	0	70
Vigneto (14)	80_95	P76	10_15	b)M						-3.01	-1.95	-1.18	4.01	4.06	4.16	1.30	1.80	3.00	61	26	22	52
<i>Stud</i>																						
OldPortaMarina (20)	40		20	c)AL			1.0	1.0	10 (tiles)													
OldPortaMarina (20)	40		20	b)CS																		
Scarp lava (25a)	177		25	c)AL																		
Scarp lava (25a)	177	P105	152	b)ULB						-3.27	-1.56	-0.47	3.69	4.03	4.14	1.52	2.11	2.79	72	20	64	17
Scarp lava (25a)	177	P104		b)ULB	100	30			30 (logs)	-3.54	-2.69	-1.79	2.98	3.76	4.10	0.68	0.95	3.23	58	13	28	59
Scarp lava (25a)	177	P103		b)ULB	500	13	3.0	2.0	15 (tiles)	-4.06	-3.78	-3.56	0.01	2.09	3.76	-1.43	-2.60	2.93	25	4	65	31
Scarp lava (25b)	75		10	c)AL																		
Scarp lava (25b)	75	P102	65	b)M			1.6	1.6		-3.11	-2.39	-1.68	4.01	4.06	4.17	1.03	1.41	3.23	57	28	28	45
Porta Stabia (21)	27_83		9_30	c)AL																		
Porta Stabia (21)	27_83		8_23	b)CB	330	7																
Porta Stabia (21)	27_83		5_15	b)PP																		
Porta Stabia (21)	27_83	P6	5_15	b)M	80	5	1.6	1.7		-2.82	-1.09	0.12	4.02	4.07	4.17	1.94	2.85	2.58	76	30	13	57
Necropolis (22c)	100	P45	100	b)ULB						-3.09	-2.39	-2.01	1.61	3.43	4.10	0.05	-0.90	2.91	35	13	37	50
Necropolis (22c)	100	P44		b)ULB						-3.86	-3.30	-2.90	1.15	3.45	4.09	-0.53	-1.75	3.37	29	12	55	33
Necropolis (22b)	45_50	Po-45	13_18	c)AL						-2.31	-0.23	0.99	4.02	4.07	4.17	2.12	2.53	2.15	82	30	10	60
Necropolis (22b)	45_50	Po-44	17	b)CB	110	20				-0.23	0.90	1.58	4.00	4.05	4.16	2.62	2.92	1.58	94	25	1	73
Necropolis (22b)	45_50	Po-43	7	b)PP					10 (tiles)	-2.60	-1.30	0.08	3.73	4.03	4.14	1.68	2.31	2.66	76	20	15	64
Necropolis (22b)	45_50	Po-42	8	b)M			1.8	1.9		-2.75	-1.30	-0.78	3.52	4.02	4.14	1.34	1.29	2.66	63	19	13	68
Necropolis (22d)	50		20	c)AL																		
Necropolis (22d)	50		14	b)CB																		
Necropolis (22d)	50		6	b)PP																		
Necropolis (22d)	50		10	b)M			1.1	1.3														
Necropolis (22a)	46_51		7	c)AL																		
Necropolis (22a)	46_51		7_11	c)AL + PP	220	20																
Necropolis (22a)	46_51		19	b)CB																		

Table 3. (continued)

Site and Section	Bed <sub>0</sub> cm	Sample	Facies <sub>0</sub> cm	Facies	L, cm	H, cm	MP, cm	ML, cm	MB, cm	$\phi_5$ , $\phi$	$\phi_{16}$ , $\phi$	$\phi_{25}$ , $\phi$	$\phi_{75}$ , $\phi$	$\phi_{84}$ , $\phi$	$\phi_{95}$ , $\phi$	Mz, $\phi$	Md $\phi$ , $\phi$	$\sigma\phi$ , $\phi$	F1, %	F2, %	L, %	CA, %
Necropolis (22a)	46_51		8	b)PP																		
Necropolis (22a)	46_51		5	b)M			1.6	2.1														
Iozzino (26)	70		16	c)AL																		
Iozzino (26)	70		37	b)CB	190	23																
Iozzino (26)	70		10	b)PP																		
Iozzino (26)	70		7	b)M																		
<i>West</i>																						
Scarp_ViaFarnacista (16)	80		20	c)AL																		
Scarp_ViaFarnacista (16)	80		60	b)CS			1.0	1.0	wall													
Outside_ViaFarnacista (17)	32_75		10_15	c)AL																		
Outside_ViaFarnacista (17)	32_75		9_52	b)CB	50	20																
Outside_ViaFarnacista (17)	32_75		8	b)M			1.6	2.1														
Outside_soprastanti (18)	14_70		4_10	c)AL																		
Outside_soprastanti (18)	14_70		2_52	b)SCF																		
Outside_soprastanti (18)	14_70		8	b)M			2.0	3.2	10 (tiles)													
Scarp_Soprintendenza (19)	107_117		14	c)AL																		
Scarp_Soprintendenza (19)	107_117		33	b)SCF																		
Scarp_Soprintendenza (19)	107_117		50_60	b)SCF	120	11																
Scarp_Soprintendenza (19)	107_117		10	b)CS			1.9	4.0	80 (log) 10 (tiles)													

<sup>a</sup>Symbols are Bed<sub>0</sub>, bed thickness variation; sample, collected sample; facies<sub>0</sub>, facies thickness variation; facies, facies of each single subunits (nomenclature as in Figure 5); L, length of dune or lenses; H, height of dune or lenses; MP, maximum pumice diameter; LM, maximum lithic diameter; MB, maximum debris diameters (tiles, piece of wall, logs eroded by the PDC);  $\phi_5$  up to  $\phi_{95}$ , percentile; Mz, mean diameter [from *Folk and Ward*, 1957]; Md $\phi$ , mean diameter;  $\sigma\phi$ , sorting [from *Inman*, 1952]; F1, weight percentage of fractions finer than 1 mm; F2, weight percentage of fractions finer than 1/16 mm; L, weight percentage of lapilli; CA, weight percentage of coarse ash.

Table 4. Grain Size and Facies Data Analyses of EU7pf Deposits<sup>a</sup>

Site and Section	Bed <sub>i</sub>	Sample	Facies <sub>to</sub> cm	Facies	MP, cm	ML, cm	$\phi$ 5, $\phi$	$\phi$ 16, $\phi$	$\phi$ 25, $\phi$	$\phi$ 75, $\phi$	$\phi$ 84, $\phi$	$\phi$ 95, $\phi$	Mz, $\phi$	Md $\phi$ , $\phi$	$\sigma\phi$ , $\phi$	F1, %	F2, %	L, %	CA, %
<i>Nord</i>																			
Antonio (1a)	20		10	c)AL															
Antonio (1a)	20		10	b)CS	1.5	1.2													
Antonio (1b)	14		10	c)AL															
Antonio (1b)	14		4	b)CS	1.5	1.2													
Villa Misteri (2a)	11		6	c)AL															
Villa Misteri (2a)	11	P86	5	b)M	0.80	1.3 (4)	-1.43	-0.16	0.65	4.02	4.07	4.17	2.14	2.50	2.11	82	28	5	67
Villa Misteri (2c)	20		15	c)AL															
Villa Misteri (2c)	20		5	b)M	0.5	1.8	-1.35	0.38	1.19	4.02	4.07	4.17	2.40	2.81	1.87	86	29	4	67
Villa Misteri (2c)	20	P11	5	b)M															
Via delle Tombe (23)	19		10	c)AL	0.5	0.5													
Via delle Tombe (23)	19		9	b)M															
Villa Diomede (3)	30		10	c)AL															
Villa Diomede (3)	30		10	b)PP															
Villa Diomede (3)	30		10	b)M	0.5	0.5													
Villa Diomede (3)	30		13_16	c)AL															
Porta Ercolano (4)	16_24		3_8	b)CB	0.5	0.5													
Porta Ercolano (4)	16_24		13	c)AL															
P.Erc-P.Ves (5a)	18		5	b)M	0.5	0.8													
P.Erc-P.Ves (5a)	18		20	c)AL															
Porta Capua (6)	25		5	b)M	0.5	0.8													
Porta Capua (6)	25		8	c)AL															
Porta Nola (7a)low	19		11	b)M	3.0	1.7													
Porta Nola (7a)low	19		8	c)AL															
Porta Nola (7a)high	19		11	b)M	3.0	1.7													
Porta Nola (7a)high	19		10	c)AL															
Porta Nola (7b)	16		6	b)M	3.0	2.0													
Porta Nola (7b)	16		5	c)AL															
NE circumvesuviana (8a)	6_7		1_2	b)M	0.8	1.1													
NE circumvesuviana (8a)	6_7		5	c)AL															
NE circumvesuviana (8b)	6_7		1_2	b)M	1.0	1.0													
NE circumvesuviana (8b)	6_7		5	c)AL															
NE circumvesuviana (8c)	6_7		1_2	b)M	1.0	1.0													
NE circumvesuviana (8c)	6_7		10_13	c)AL															
Via Vesuvio (10)	15_26		5_13	b)M	0.9	0.8	-2.72	-1.51	-0.82	3.91	4.05	4.16	1.26	1.25	2.78	63	24	16	60
Via Vesuvio (10)	15_26	P50	10	c)AL															
Casti amanti (11a)	16		6	b)M	1.1	1.4	-2.20	-0.40	0.39	4.05	4.10	4.19	2.24	3.03	2.25	79	36	8	56
Casti amanti (11a)	16	P60	11	c)AL															
Casti amanti (11d)	17		6	b)M	1.0	1.2													
Casti amanti (11d)	17		11	c)AL															
Via Castircio (12a)high	17		6	b)M	1.0	1.5													
Via Castircio (12a)high	17		11	c)AL															
Via Castircio (12a)low	17		6	b)M	1.0	1.5													
Via Castircio (12a)low	17		12	c)AL															
Via Castircio (12c)	18		6	b)M	0.9	1.5	-2.62	-0.88	0.14	4.03	4.08	4.18	2.01	2.82	2.48	76	31	12	57
Via Castircio (12c)	18	P53	7	c)AL															
Via dell'Abbondanza (24)	11		4	b)M	1.2	1.3													
Via dell'Abbondanza (24)	11		3	c)AL															
Vigneto (14)	12		9	b)M	1.2	1.3													
Vigneto (14)	12																		



Table 4. (continued)

Site and Section	Bed <sub>i</sub>	Sample	Facies <sub>t</sub> cm	Facies	MP, cm	ML, cm	$\phi_5$ , $\phi$	$\phi_{16}$ , $\phi$	$\phi_{25}$ , $\phi$	$\phi_{75}$ , $\phi$	$\phi_{84}$ , $\phi$	$\phi_{95}$ , $\phi$	Mz, $\phi$	Md $\phi$ , $\phi$	$\sigma\phi$ , $\phi$	F1, %	F2, %	L, %	CA, %
<i>Sud</i>																			
OldPortaMarina (20)	17		10	c)AL															
OldPortaMarina (20)	17		7	b)M	0.5	1.5													
Scarp lava (25a)	11		6	c)AL															
Scarp lava (25a)	11		5	b)M	0.5	1.7													
Scarp lava (25b)	11		6	c)AL															
Scarp lava (25b)	11		5	b)M	0.5	1.7													
Stabia (21)	15		10	c)AL															
Stabia (21)	15		5	b)M	0.8	1.2													
Necropolis (22b)	17		10	c)AL															
Necropolis (22b)	17	Po-48	7	b)M	0.5	0.5	-1.63	-0.30	0.55	3.72	4.03	4.14	2.10	2.58	2.17	81	20	6	74
Necropolis (22a)	11		5	c)AL															
Necropolis (22a)	11		6	b)M	1.4	1.5													
Iozzino (26)	0																		
<i>West</i>																			
Scarp_ViaFarmacista (16)	18		13	c)AL															
Scarp_ViaFarmacista (16)	18		5	b)M	1.5	2.0													
Outside_ViaFarmacista (17)	13_23		10_18	c)AL															
Outside_ViaFarmacista (17)	13_23		3_5	b)M	1.4	2.1													

<sup>a</sup>Symbols are Bed, bed thickness variation; sample, collected sample; Facies, facies thickness variation; facies, facies of each single subunits (nomenclature as in Figure 5); MP, maximum pumice diameter; LM, maximum lithic diameter;  $\phi_5$  up to  $\phi_{95}$ , percentile; Mz, mean diameter [from *Folk and Ward*, 1957]; Md $\phi$ , mean diameter;  $\sigma\phi$ , sorting [from *Inman*, 1952]; F1, weight percentage of fractions finer than 1 mm; F2, weight percentage of fractions finer than 1/16 mm; L, weight percentage of lapilli; CA, weight percentage of coarse ash.

**Table 5.** Deposit Nomenclature<sup>a</sup>

Parameter	Value
Bed thickness, cm	
Very thin beds	1–3
Thin beds	3–10
Medium beds	10–30
Thick beds	30–100
Very thick beds	>100
Grain diameter, mm	
Fine-grained ash	<0.063
Medium -grained ash	0.063–0.5
Coarse-grained ash	0.5–1
Very coarse-grained ash	1–2
Fine-grained lapilli	2–4
Medium-grained lapilli	4–16
Coarse-grained lapilli	16–64
Fine-grained blocks	64–256
Coarse-grained blocks	>256
Sorting $\sigma\phi$	
Very well sorted	0–1
Well sorted	1–2
Poorly sorted	2–4
Very poorly sorted	>4

<sup>a</sup>Nomenclature used in the text for bed thickness, grain size, and sorting of the pyroclastic deposits [from *Sohn and Chough*, 1989].

[13] Finally, the Geographical Information System, GIS, of the excavations of ancient Pompeii, devised by *Giannini et al.* [2000], allowed the urban parameters (average wall height of the houses, building size and spacing) to be calculated both of ancient Pompeii and modern Pompei.

#### 4. PDC Flow Directions and Emplacement

[14] Pompeii was built on a low hill with a maximum height of 30 m above sea level and a ~10-m scarp on its western edge (Figure 6). This topography was sufficient to strongly influence the basal flow directions and thickness of the PDC deposits (Figure 1a). However, the flow directions were also significantly disturbed by the urban settlement itself (Figure 6). This was represented by buildings of relatively low and uniform heights, having an average height of  $3.6 \pm 1.6$  m. The highest buildings and towers had maximum heights of 8 m, while the city wall was in some places 10 m high. Following partial burial by a 2.5-m-thick pumice blanket, the urban topography had an average height of 1.8 m, with the highest points protruding 7 m above the fallout deposits.

[15] As explained previously, the pole of the magnetic foliation plane is considered as a proxy for the flow direction of the PDCs. Figure 6 shows the EU4pf flow direction at each site; the color of the arrow depends on the geometric relation between the site direction and the general flow direction, coming from about  $340^\circ$  and flowing toward  $160^\circ$ , as inferred from the vent location (Figure 1). The black arrows (vent flow) represent directions close to the general one and mainly occur at sites located in the open country around the city. The hollow arrows (structure-parallel) represent directions that follow the main structures of the city: the walls and the road network. The blue arrows (local turbulence) are related to localized but abrupt changes in the paleotopographical surface, due to combination of roads (low) and walls (high) or local outcrops of ancient lava flow on which the town was built. The orange arrows (random) are directions that deviate strongly from the main

flow direction and appear to point in random directions. These typically are found in material deposited inside the buildings. This flow direction grouping is reflected by different properties of the magnetic fabric in the four categories (Table 1). The mean value of the degree of anisotropy ( $P$ ) of the random sites is 1.013. This is lower than the mean values of the other groups,  $P = 1.017$  and is probably related to the high turbulence that the PDCs experienced at some localities in this group. In the majority of the vent flow and structure-parallel sites, the magnetic fabric is well defined (type A, Figure 4). For these groups the foliation pole and lineation are imbricated upflow, as is typical of the normal fabric (Figure 3a), and their azimuths are close to each other. In contrast, the fabric for the majority of the local turbulence and random sites is not so well defined. In these cases the lineation is mainly dispersed within the foliation plane (type B, Figure 4) and the lineation azimuth is generally orthogonal to that of the foliation pole.

[16] The directions indicated by the macrofabric elements, when present, agree with those of the magnetic analysis (Figure 7). The poles of the largest plane of the tiles show the same orientations as those of the  $k_{\min}$  axes. At a few sites, charcoal and tree logs were founded arranged parallel to the magnetic lineation (Figures 7b, 7c, and 7d), although two were orthogonal (at site 5, Figure 7a). The results from site 12b (Figure 7c) are particularly interesting. This site shows the lowest value for the degree of anisotropy (1.005) and the magnetic foliation is poorly defined; the E3-2 radius of confidence was the highest encountered ( $55.7^\circ$ , Table 1). The indications of the magnetic fabric alone would thus be considered very weak and their interpretation hardly reliable. The results, however, agree with those obtained from the macrofabric elements (Figure 7c): the  $k_{\min}$  axes are dispersed around the tile poles, whereas the  $k_{\max}$  axes are close to the logs' direction. Notwithstanding the low anisotropy the geometry of the fabric still reflects the depositional characteristics.

#### 5. PDC Deposits Around and Within Pompeii

[17] The AMS data show that the presence of the town not only strongly affected the flow directions, but also the deposition of the first two PDCs that reached and entered the town. These effects are highlighted by local variations in the deposit geometry, texture and facies associations.

##### 5.1. EU3pf

[18] The EU3pf deposit in Pompeii was emplaced by a dilute PDC derived from a denser proximal PDC that, 4 km from the vent, left a 5-m-thick, coarse-grained deposit [*Gurioli et al.*, 1999]. In Pompeii the EU3pf deposits range in thickness from 4 to 30 cm and show wide variation on the scale of a single outcrop (Figures 8a and 9a). The EU3pf deposits within Pompeii, and throughout the plain south of Vesuvius [*Cioni et al.*, 1992], show a sequence of at least 3 subunits (Figure 8a). These were interpreted by *Gurioli et al.* [1999] as resulting from the sedimentation of a single, sustained yet, unsteady, nonuniform PDC. These subunits reflect the fluctuations inherent during sustained column collapse, followed by deceleration and sedimentation of the current itself [*Gurioli et al.*, 1999]. Subunit I is a gray

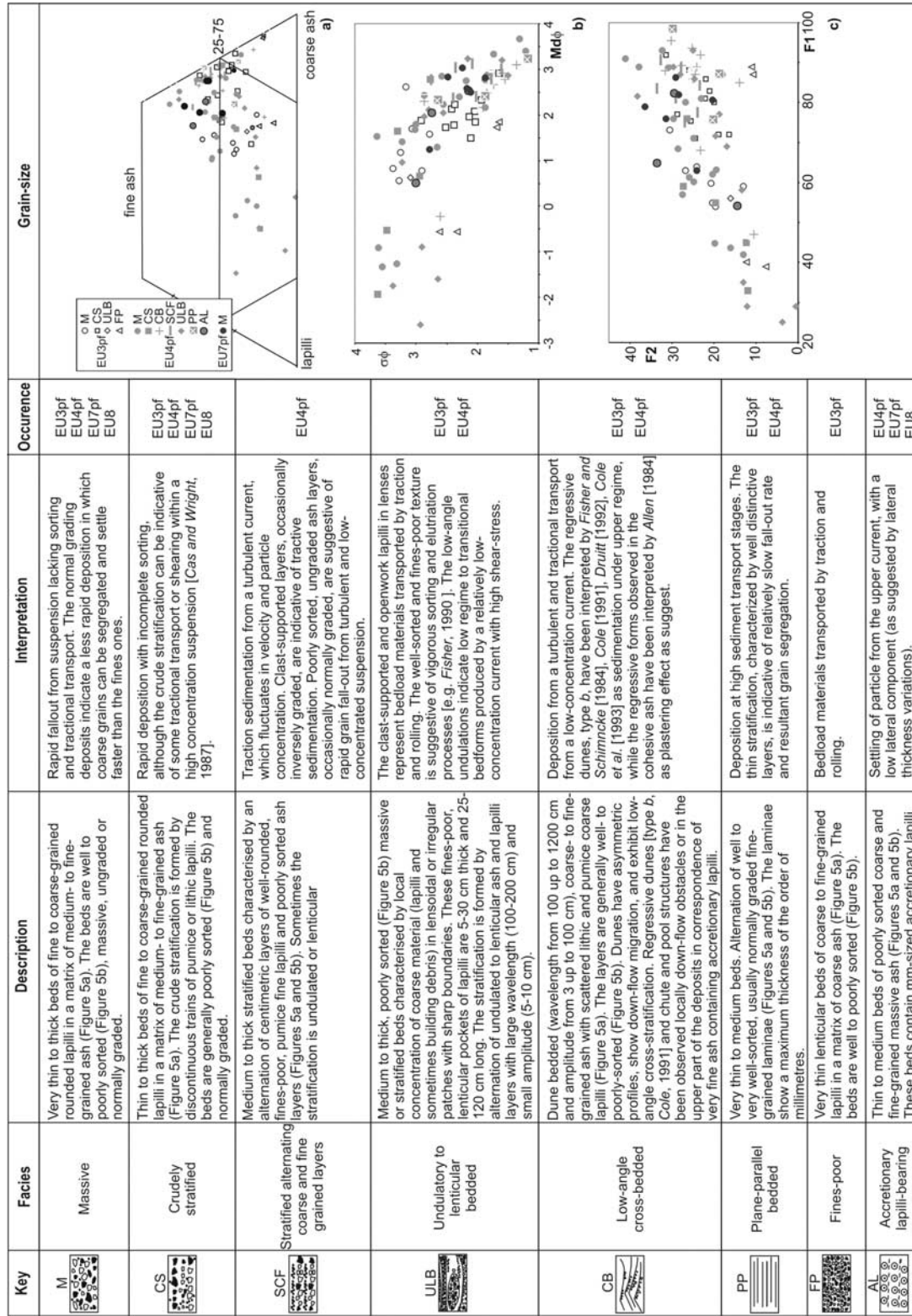


**Figure 5.** Schematic table of the description, interpretation, and occurrence of the eight main facies of the pyroclastic deposits at Pompeii. Grain size features are represented by (a) three-component grain size variations; (b) sorting ( $\sigma\phi$ ) versus median grain size ( $Md\phi$ ); (c) the weight percent finer than 1/16 mm ( $F_2$ ) versus the weight percent finer than 1 mm ( $F_1$ ).



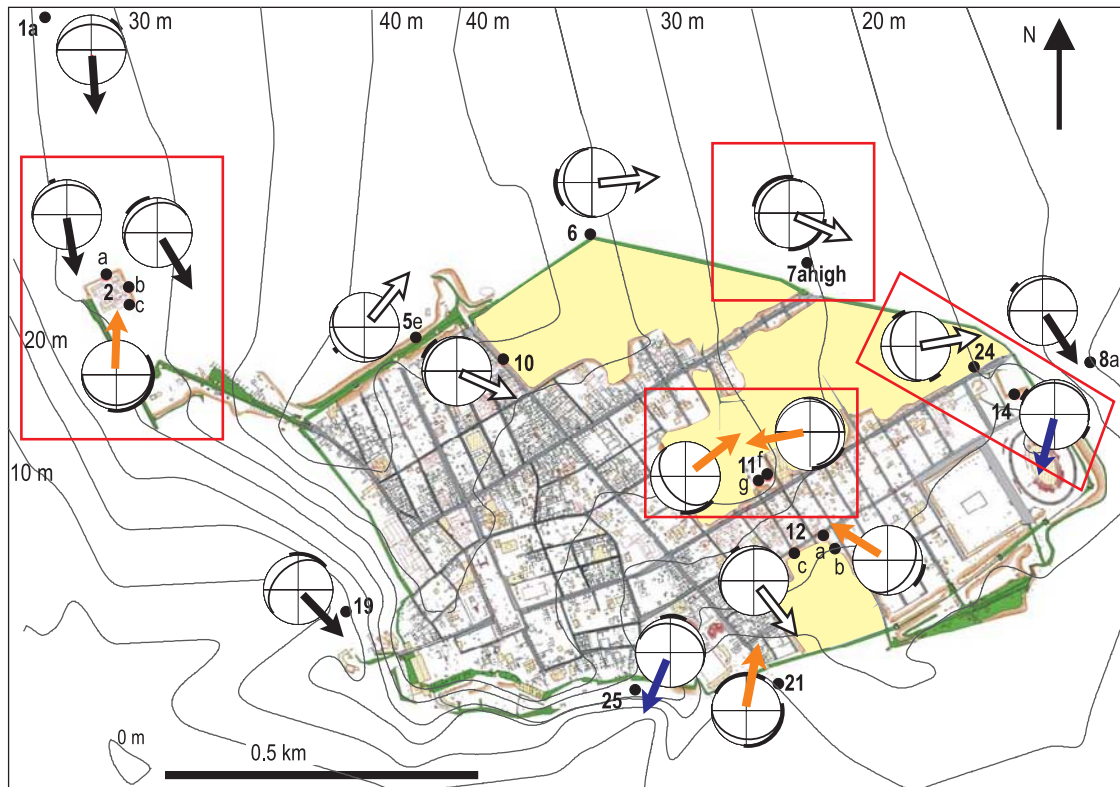


**Figure 6.** Flow directions of EU4pf PDC as inferred from AMS measurements. Paleocontours (m) before A.D. 79 eruption are in black, dots indicate sampling sites. Symbols in equal-area projections: great circles indicate magnetic foliation; bold part of the base circle indicates azimuth of magnetic lineation as defined by the ellipse of confidence; large arrow indicates site-mean flow direction (see text for color explanation).

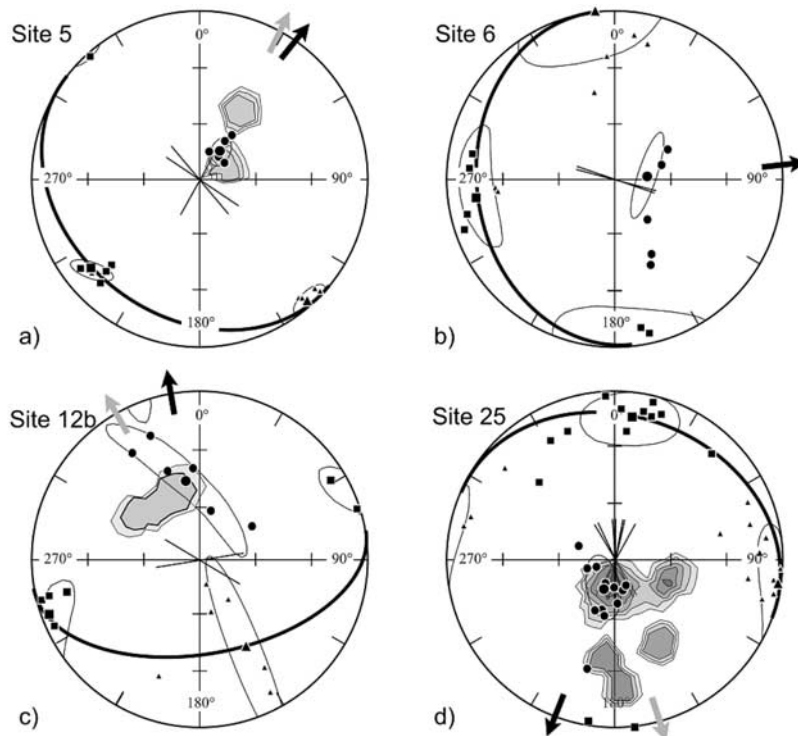


**Figure 7.** Comparison between flow directions inferred from AMS (black arrows), directions of tree log (straight lines) and tile poles (gray arrows). Symbols are as in Figure 3.



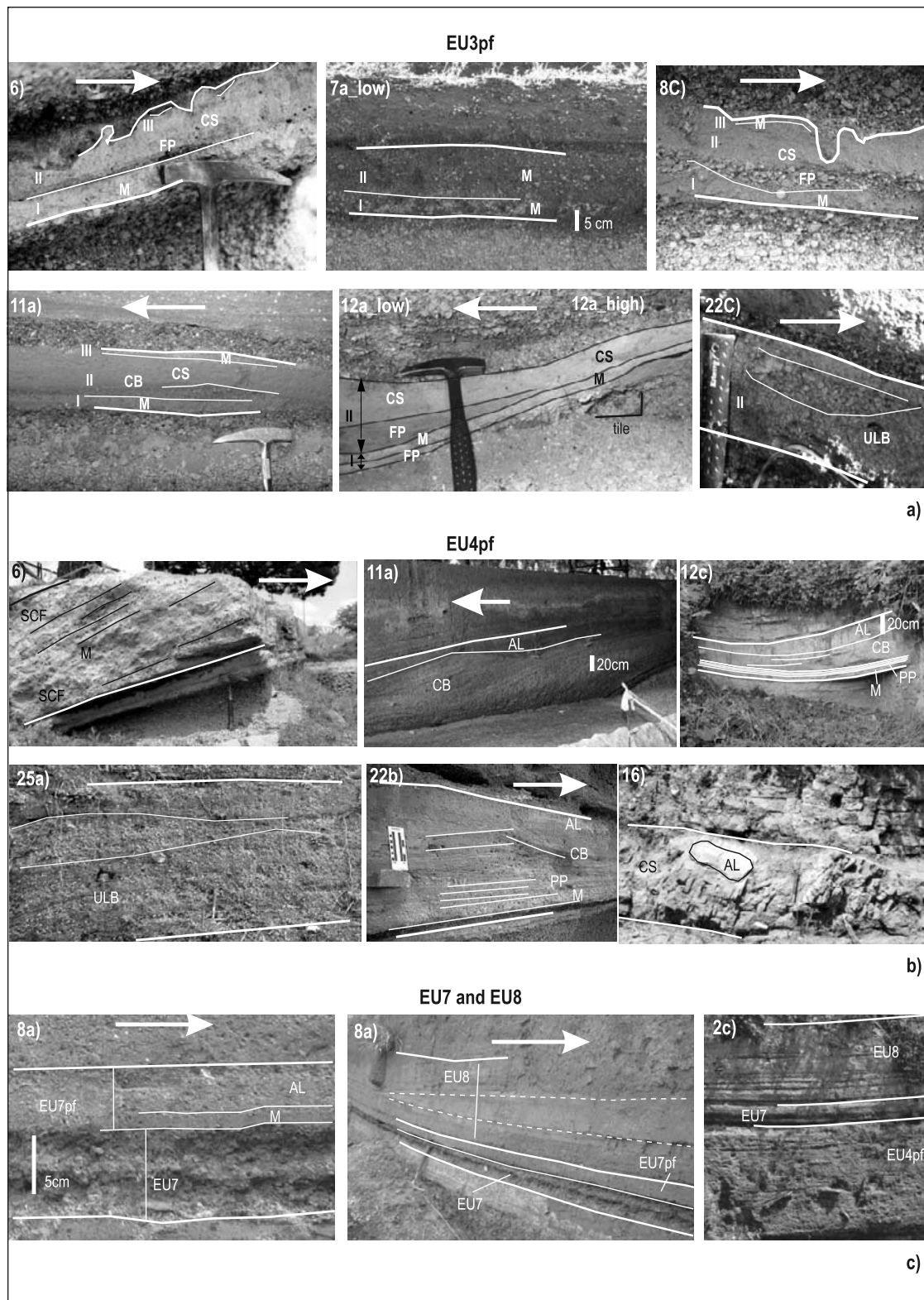


**Figure 8.** Sedimentary facies of (a) EU3pf, (b) EU4pf, and (c) EU7pf and EU8 deposits. Photos show vertical and lateral facies association in the units at different sites. Numbers on the top left indicate sites; arrow indicates main flow direction.

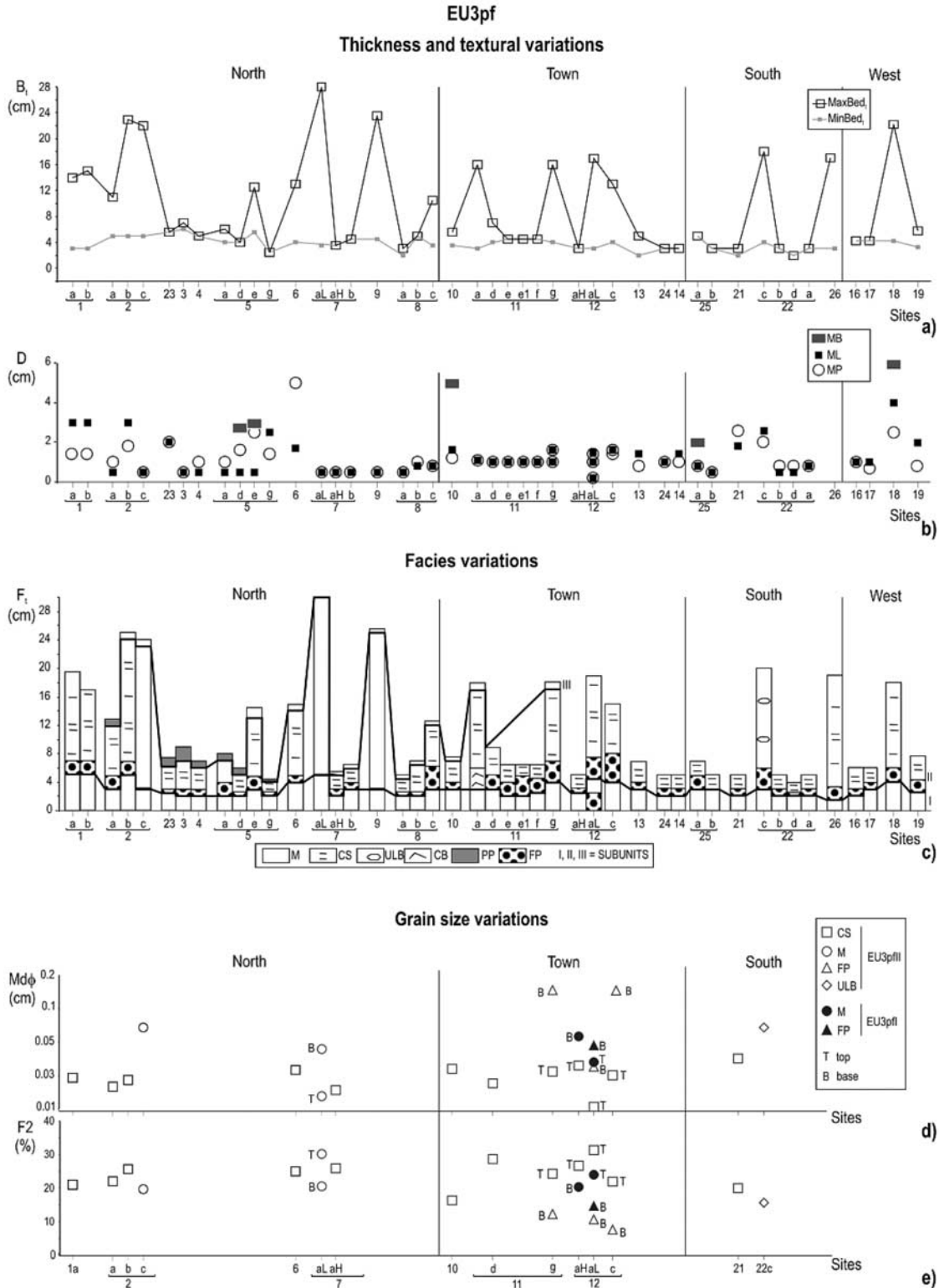


**Figure 9.** Measured parameter variations in the EU3pf deposits versus distance (sites, where H is topographic high, L is topographic low) across the town, plotted parameters being (a) Max Bed<sub>t</sub>, maximum bed thickness; Min Bed<sub>t</sub>, minimum bed thickness; (b) MB, maximum diameters for building fragments; ML, maximum diameters for lithics; MP, maximum diameters for pumice, in EU3pfII crudely stratified facies; (c)  $F_t$ , facies thickness for EU3pf subunits I, II, and III (see Figure 5 for facies nomenclature); (d)  $Md\phi$ , medium grain size; and (e) F2, fine ash content. For site location, see Figure 1b.

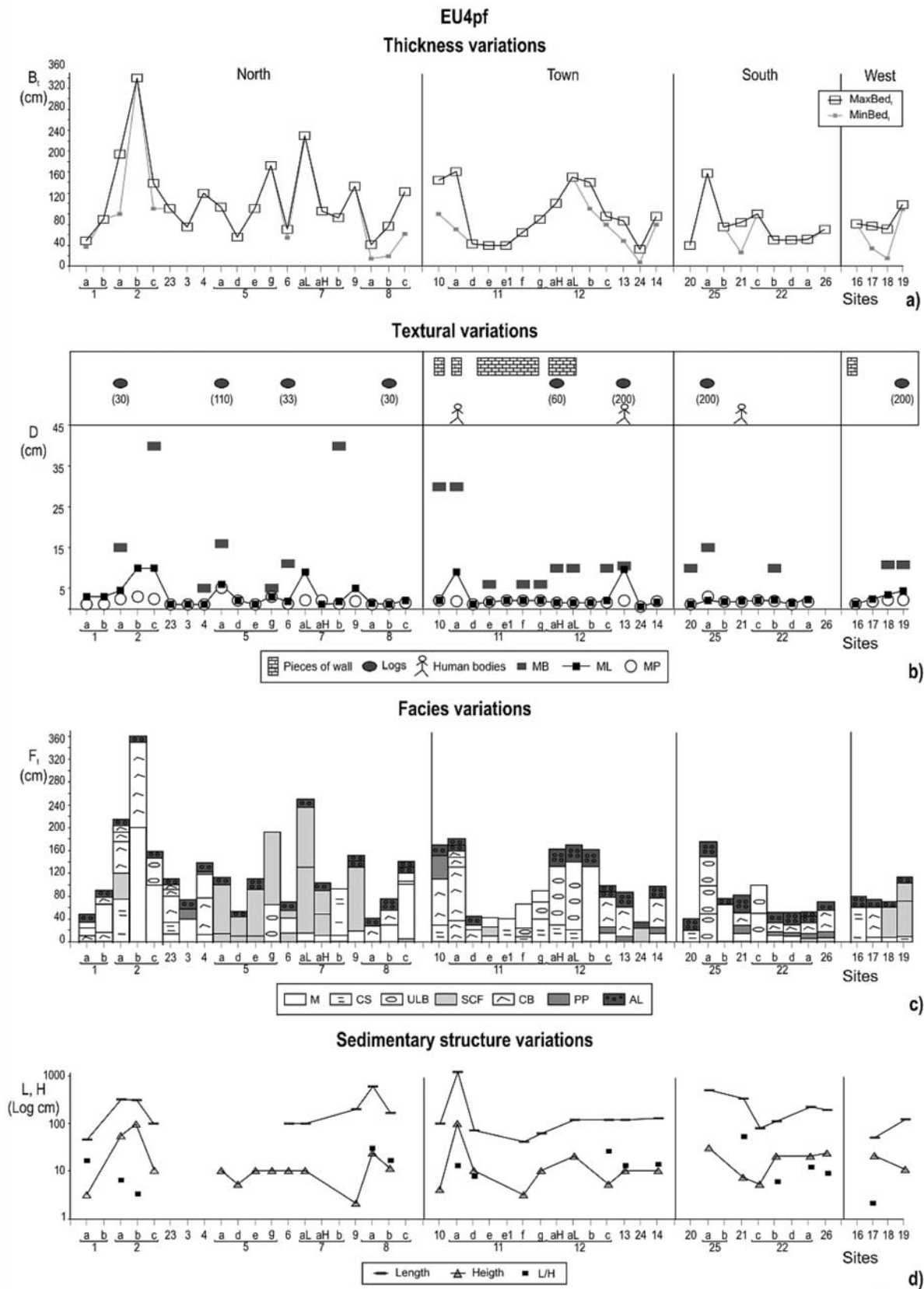


Figure 10



yellow ash layer ranging from 1 to 5 cm in thickness (Figure 8a and Table 2). It is composed mainly of massive facies (Figures 8a and 9c) that on the outcrop scale shows a constant thickness. Only at one site (site 12a\_low, Figure 8a) can this subunit be split into two facies: fines poor followed by massive. This split occurs after an obstacle represented by a 2 cm high tile. Subunit II is a light yellow ash layer that displays the widest facies and thickness variations (Figures 8a and 9c). A general fining upward trend is ubiquitous recorded in this subunit (Figure 9d). Within Pompeii, across flat surfaces, this deposit comprises a vertical association of fines poor followed by crudely stratified facies with an average thickness of 6 cm (sites 6 and 12a\_high, Figures 8a and 9c and Table 2). However, where the PDC encountered obstacles, such as at sites where the deposit filled roads or upstream of walls, the maximum thickness reached 25 cm (site 7a\_low, Figure 8a). Locally, the two vertical facies (fines poor and crudely stratified) can pass to a coarse grained massive facies, as where the deposit filled a road (site 7a\_low, Figure 8a). It can also develop an undulatory lenticular bedded facies, as after encountering an abrupt downward step in the bed topography of a few meters height (site 22c, Figure 8a). Down flow of smaller obstacles, only the fines-poor facies shows any increase in thickness or grain size (sites 8c and 12a\_low, Figure 8a), or grade into the cross-bedded facies (site 11a, Figure 8a). The competence (ML and MP) and capacity (MdΦ) of this subunit increase only locally, while their mean values do not show substantial variation across the town (Figures 9b and 9d). Subunit III is a brown yellow layer (Figure 8a) that comprises plane parallel to massive facies. This unit is disturbed by impact sags from the overlying fallout unit (sites 6 and 8c, Figure 8a), but otherwise its thickness of 0.5 to 1 cm is almost constant. This layer disappears in the south sector of Pompeii and south of Pompeii.

[19] Subunit I was emplaced from the initial collapse of the column [Gurioli *et al.*, 1999]. Its sedimentation features at Pompeii are those of a waning current in which the particles were emplaced at high fallout rates from a suspension in which the turbulence was almost suppressed. This is indicated by the poor sorting of massive facies. However, locally, low-amplitude (~2 cm high) surface irregularities were able to cause a flow transformation that induced a rapid segregation of the coarsest particles at the base of the flow (12a\_low site, Figures 8a, 9c, 9d, and 9e). Emplacement of subunit II occurred during the peak of the column fountaining activity, and was thus emplaced by a more energetic current than subunit I [Gurioli *et al.*, 1999]. The fines-poor and crudely stratified vertical facies association represents the sedimentation from a waning stratified, dilute, current. The basal fines-poor facies can be interpreted as a tractional bed load. The crudely stratified facies of the upper part of the deposit is indicative of rapid

deposition with incomplete sorting, although the crude stratification is indicative of some tractional transport. The dense, lower part of the current was able to interact locally with small, 2 to 4 cm high, obstacles. At such locations the current experienced an increase in its shear velocity and emplaced coarser material downflow of the obstacles, as suggested by the thicker and coarser fines-poor facies (site 8c, Figure 8a). The rare occurrence of low-angle cross lamination (site 11a, Figure 8a) in the deposits suggests occasional decreases in the sedimentation rate of the current and its capability to deposit in a tractional regime. When the obstacle heights exceeded 10 cm, a larger portion of material is segregated, being the current erosive upflow of the obstacle and emplacing coarse-grained massive facies or undulatory lenticular bedded facies downflow (site 7a\_low and site 22c, respectively, Figure 8a). Observed grain size increases result from the entrainment of underlying pumice and building debris (Figure 9b). However, such effects were localized and the average values of competence and capability, as well as the thickness of the unit, seem to be the same north and south of the town (Figure 9). Subunit III was emplaced during the final, least energetic phase of the column collapse. At this distance from the vent the sedimentation was from a very dilute suspension. This layer disappears toward the southern part of the town (Figure 9c), suggesting that at a distance of 10 km from the vent, it was no longer able to deposit a well-defined layer. A fine ash layer, interpreted as deposition from a trailing upper current, is apparent at some locations around Vesuvius where it lies on the top of the third subunit [Gurioli *et al.*, 1999]. However, it was not observed at this (medial) distance from the vent.

## 5.2. EU4pf

[20] Around Vesuvius, EU4pf deposits were emplaced by a turbulent stratified PDC that transported and deposited sediment in the style of a high-density turbidity current [Cioni *et al.*, 2004]. At Pompeii, the deposits display an upward fining sequence from massive to cross-stratified ash, capped by a pisolite-bearing ash bed (Figure 8b). These deposits drape Pompeii, yet thicken to a maximum of 3 m across roads or upstream of obstacles, and thin to a minimum of 0.1 m over and around walls as well as downstream of obstacles. The thickness of EU4pf decreases from the north to the south of the town, showing generally lower values on the steep slopes encountered on the western edge of the town (Figure 10a). At some sites, logs, pieces of wall, tiles and bodies have been found within these deposits (Figures 7 and 10b), mainly concentrated toward the base of the deposit. Across the surrounding plain, at this distance from the vent, the deposits usually show a turbidite-like sequence, comprising a vertical sequence of massive, plane-parallel, cross-stratified and accretionary lapilli facies [Cioni

**Figure 10.** Measured parameter variations in the EU4pf deposits versus distance (sites, where H is topographic high, L is topographic low) across the town, plotted parameters being (a) Max Bed<sub>t</sub>, maximum bed thickness; Min Bed<sub>t</sub>, minimum bed thickness; (b) MB, maximum diameters for building fragments; ML, maximum diameters for lithics; MP, maximum diameters for pumice as well as presence of logs (log lengths given in brackets), wall chunks, and human bodies in EU4pf; (c) F<sub>t</sub>, facies thickness for EU4pf (see Figure 5 for facies nomenclature); (d) L, length; H, height of sedimentary structures; L/H, aspect ratio of the dune forms. For site location, see Figure 1b.



*et al.*, 1992, 2004]. This is also apparent in some outcrops inside the ruins (e.g., site 22b, Figure 8b). However, around and inside the town, the deposits show wide facies and thickness variations that are strongly related to the urban topography. Their maximum lithic size also shows much local variation, paralleling variation in maximum building material size (Figure 10b). The stratified coarse and fine facies become predominant in the ramp-like deposits found on top of the hummocky terrain encountered immediately to the north of the city walls (site 6, Figures 8b and 10c). These hummocks represent mounds of rubbish built by the Romans outside the city walls (G. Stefani, personal communication, 2003). The same facies also occur in deposits infilling roads that run outside of the town along the northern city walls (site 7a, Figure 10c). The cross-bedded facies is fully developed, extending from the base to the top of EU4pf deposits, in an artificial channel formed by a wall-constrained road running down a short hill within the town (site 11a, Figure 8b). Where the road flattens out, the deposit becomes more fine grained, thin and shows a turbidite-like sequence (site 12c, Figure 8b). However, the channeling influence of the road on the current remains apparent from the concave form of the deposit when viewed in section across the road (site 12c, Figure 8b). The undulatory lenticular bedded facies mainly characterizes deposits found in the lee side of walls (site 2c, Figure 10c), inside rooms (sites 11f, 11g, 12a, Figure 10c) or beyond the cliffs on the southern side of the town (sites 25a and 22c, Figure 10c). The deposits also show massive or a crudely stratified facies when surrounding collapsed walls (site 16, Figure 8b). The length and height of the sedimentary structures, as well as the shape factors (length/height) of the dunes, show local variations and generally high values inside the town (Figure 10d). All vertical facies associations are topped by the accretionary lapilli bed, which generally shows a more uniform thickness than the underlying facies (Figure 10c).

[21] Variations in the mean grain size, lapilli content and percentage of fine ash are mainly confined to the basal part of the EU4pf deposits (Figure 11). It is also interesting to observe that the mean grain size variation is paralleled by a similar variation in lapilli content (Figures 11a and 11b). This grain size increase is due to the inclusion of angular white and gray pumice lapilli that have been entrained from the underlying fallout deposits. These increases are located downslope from obstacles. The strongest depletion in fine ash is found in the undulatory lenticular bedded facies that developed where the flow moved down over steps of a few meters in height, as at sites 5g, 25a and 22c (Figure 11c). These undulatory lenticular bedded deposits are located at the southern edge of the town and locally show significant increases in thickness and grain size (Figures 10a, 10c, and 11). This contrasts with a general decrease in these parameters for the deposits emplaced elsewhere across this southern zone (Figures 10a, 10c, and 11).

[22] The sedimentological features of EU4pf deposits around Vesuvius have been interpreted as being emplaced by a sustained, turbulent, stratified PDC that transported and deposited sediment in the style of a high-density turbidity current [Cioni *et al.*, 2004]. In this context the massive facies at the base of EU4pf is consistent with suspension sedimentation under rapidly waning high-concentration

conditions. The cross-stratified facies that overlie this indicate slower deposition under moderate-to-low concentration traction conditions. Finally, the uppermost accretionary lapilli facies represent fine material deposited by slow settling from the trailing upper part of the current during very late stage waning flow. The constant thickness and massive appearance of the accretionary lapilli facies (Figure 10c) suggest that this portion of the current did not experience any interaction with the urban fabric. In contrast, the underlying deposits were emplaced mainly by the lower part of the current and show fabric, geometry, textural and facies variations that were strongly influenced by the urban roughness. On the flat topography, to the north of the town, massive or crudely stratified facies were overlain by a cross-bedded facies. This vertical facies association reveals initial deposition from a dense bed load layer within which turbulence was almost suppressed. The cross-bedded facies was then emplaced during lower rates of sedimentation associated with a turbulent suspension within which traction processes were operating (sites 1a, 2a, 2b, 23, 8a, 8b, 11d and 17, Figure 10c). Vertical sequences of cross-bedded, massive and cross-bedded facies (sites 1b and 4, Figure 10c) record fluctuations in velocity and particle concentration inside the current. Where the grain size of the deposits decreased, a turbidite-like facies sequence developed (sites 10, 12c, 13, 21, 22b, 22d, 22a, and 26, Figure 10c). This suggests stable stratification inside a waning current [Druitt, 1992] in which decreases in particle concentration and fall-out rate result in increases in traction and sorting processes [Lowe, 1988]. In contrast, stratified coarse and fine facies (sites 5a–e, 6, 7a, 9, 24, 18 and 19, Figure 10c) are related to local fluctuations in velocity and particle concentration of the current caused by 1- to 2-m-high undulations. Massive or crudely stratified facies extend throughout the whole deposit wherever sudden deposition occurred, coinciding with broken walls (sites 11e–e1, Figure 10c) or breaks of slope (sites 7b, 8c, 12b, 20, 25b and 16, Figure 10c). This suggests a sudden decrease in turbulence due to an increase in particle concentration and/or a decrease in the shear velocity within the lower part of the current. In contrast, a sudden increase in the shear velocity can be caused, for example, where the flow encounters a sloping road enclosed laterally by walls (site 11a, Figure 8b). At this location, an increase in shear velocity permits traction transportation of coarse particles and emplacement of cross-bedded facies to extend throughout the deposit. However, on the lee side of 2-m-high obstacles, a massive or crudely stratified basal facies is overlain by an undulatory lenticular bedded facies (sites 2c, 5g, 11f, 11g and 12a, Figure 10c). This indicates deposition in an environment where turbulence was not suppressed, but in which emplacement of bed load material transported by traction and rolling was still possible. Five-to-ten meter high obstacles, as at the southern edge of the town, are associated with the presence of a coarse-grained, fines-depleted undulatory lenticular bedded facies (sites 25a and 22c, Figure 10c). This indicates an increase in turbulence, caused by flow over the steep break in slope represented by the cliffs at this location [Gurioli *et al.*, 2002; Gray *et al.*, 2005]. Increases in turbulence, caused by passage over the rough urban surface, are also clear from increases in the presence of internal structures (Figures 8b, 10c, and 10d). For example,

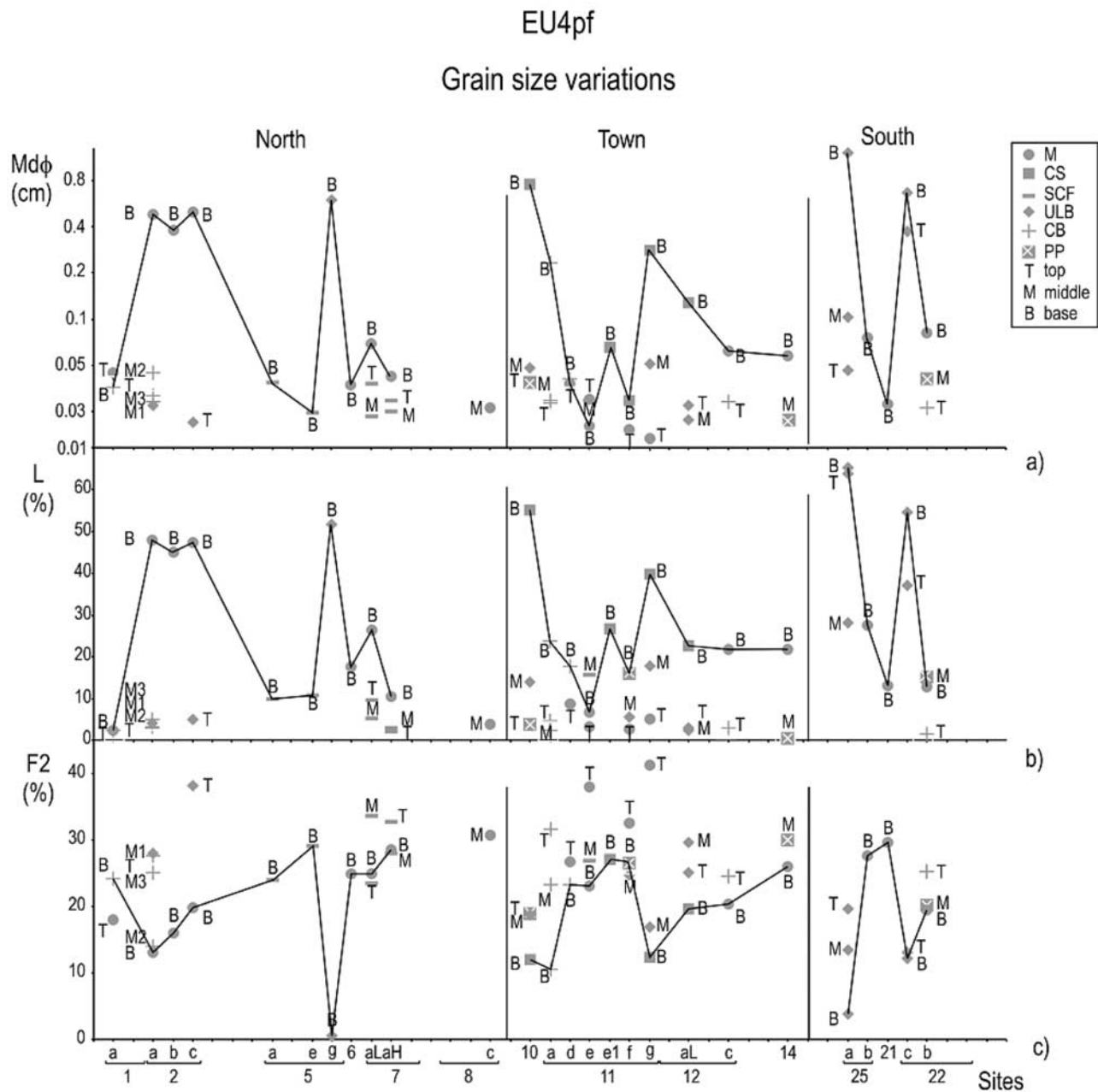


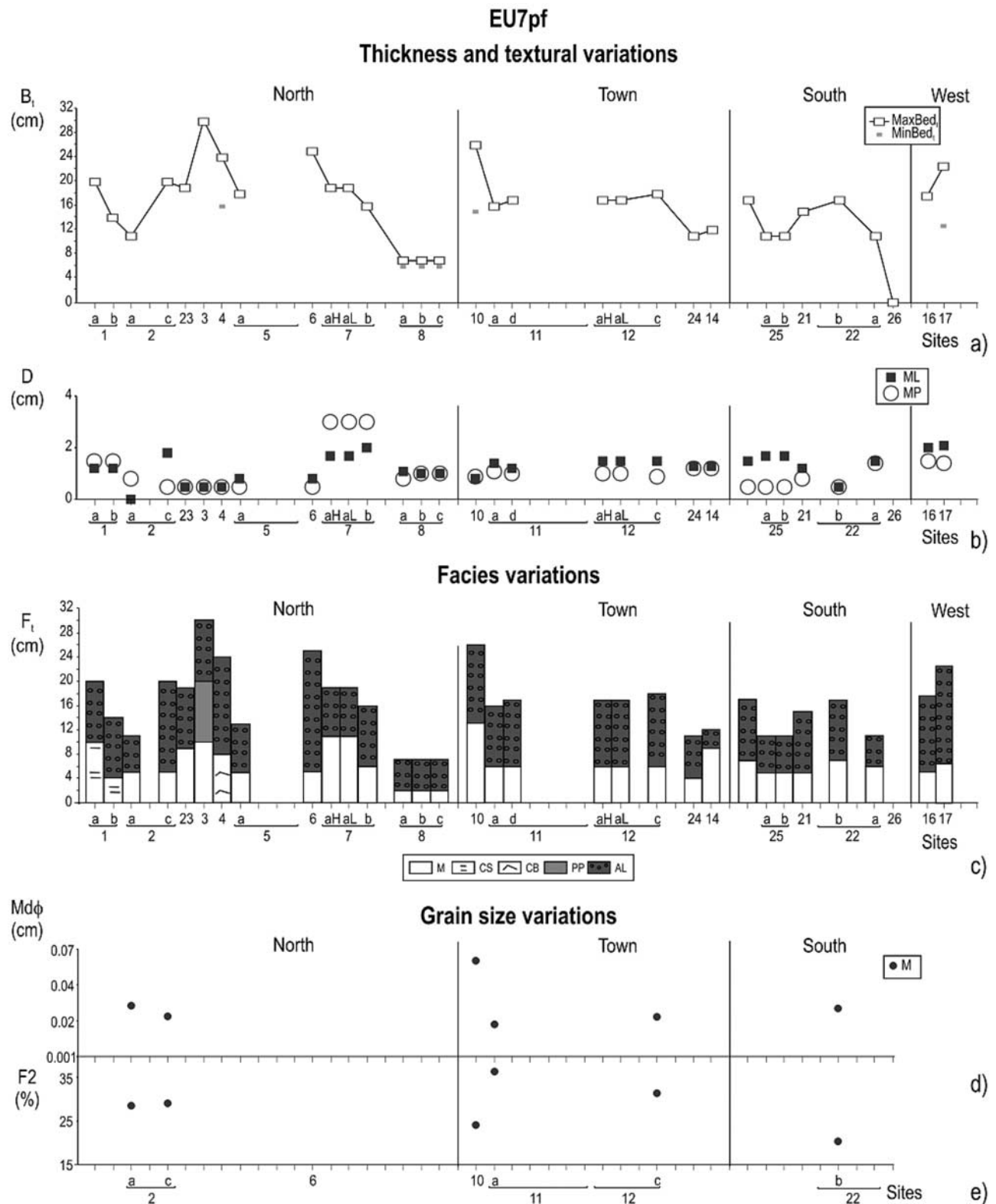
**Figure 11.** Grain size characteristic of EU4pf deposits (see Figure 5 for facies nomenclature). (a)  $Md\phi$ , medium grain size, (b)  $L$ , lapilli content, and (c)  $F2$ , fine ash content variations in the deposits versus distance (sites, where H is topographic high and L is topographic low) across the town. The lines correlate the samples at the bottom of the deposits. For site location, see Figure 1b.

the shape factor of the dunes tends to increase inside the town, suggesting an increase in turbulence. However, the highest ratio between dune length and height is found at site 21 (Figure 10d). Here the current passed through an arch, where channelization effects probably increased its velocity [Gurioli *et al.*, 2005]. The competence of the current also increased locally, in places being able to transport lithic or tile fragments ten times larger than the average size (Figure 10b and Table 3). Its dense basal portion was able to transport bodies, logs and tiles (Figure 10b) that were typically aligned parallel to the flow (Figure 7). This is

indicative of deposition from a concentrated grain dispersion in which grain inertia effects were dominant [e.g., Rees, 1983; Postma *et al.*, 1988; Hughes and Druitt, 1998]. However, some bodies, logs and tiles were aligned orthogonal to the flow (as at site 7a, Figure 3b, and site 11a, Figure 8b), showing emplacement from the traction load [e.g., Smith, 1986; Bryan *et al.*, 1998].

### 5.3. EU7 and EU8

[23] The EU7 sequence comprises two centimetric grain-supported, lithic-rich lapilli beds, separated by a cohesive



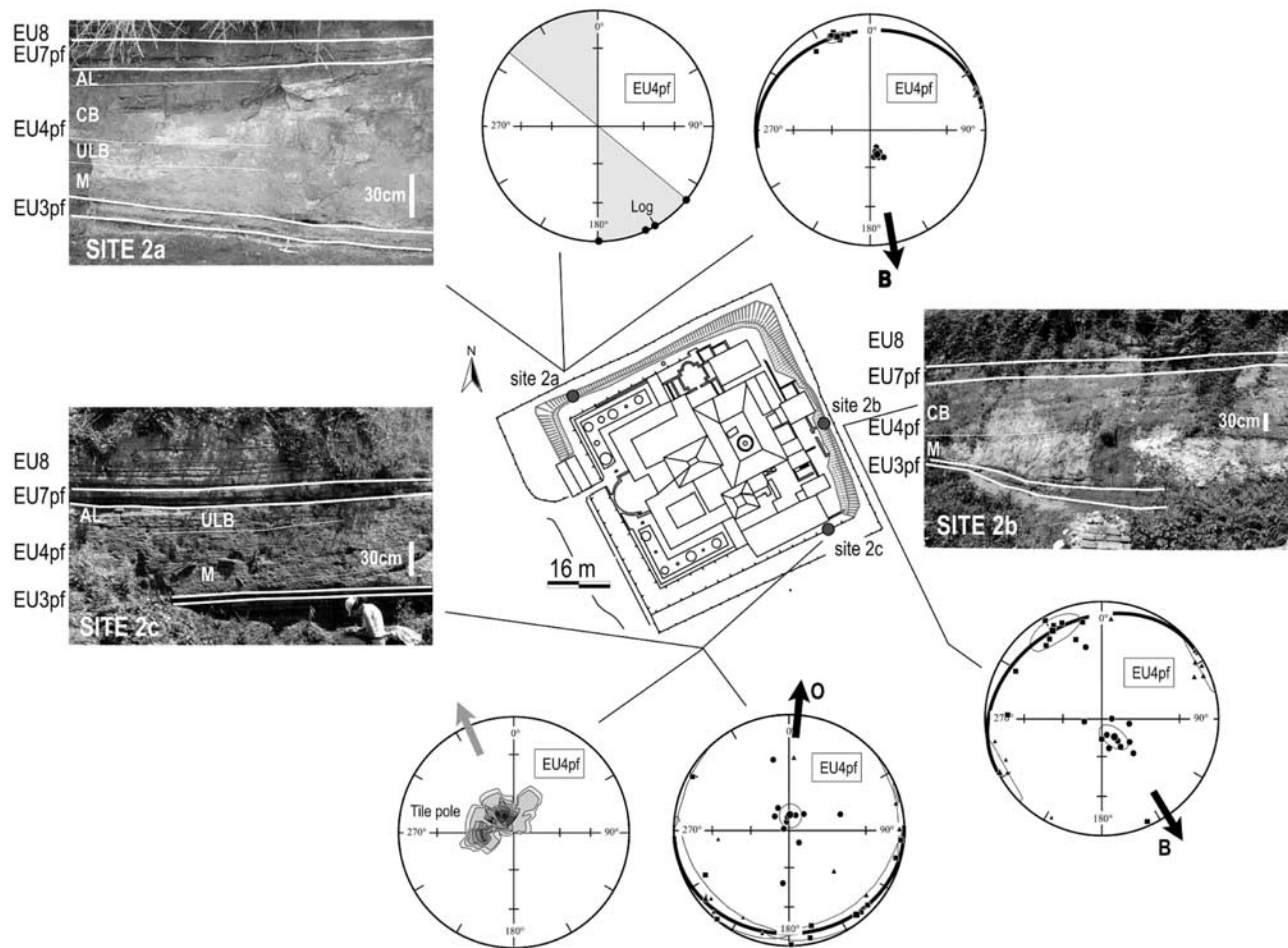


**Figure 13.** Variations in EU4pf flow directions upflow, along flow, and downflow Villa dei Misteri (VM). For each sampling site (dots in the sketch) the photo of the deposits (symbols of the facies are as in Figure 5), the stereographic projection of AMS, and macroscopic indicators (symbols as in Figure 3) are given. Bold letters close to the arrows refers to the color in Figure 6 (B, black; O, orange). For site 2a (upflow VM), both magnetic lineation and foliation and tree logs directions are concordant with the main flow direction. For site 2b (along VM), inferred directions run parallel to the VM wall. For site 2c (downflow VM), both magnetic foliation pole and tiles pole show an upflow direction. The EU4pf magnetic lineation is dispersed within the magnetic foliation plane.

ash layer (1–3 cm thick), and capped by EU7pf deposits. The EU7pf deposits comprise a coarse ash layer, topped by a massive pisolite bearing fine ash bed (e.g., site 8a, Figure 8c). The thickness of EU7pf varies from site to site, probably in response to the new topography created by EU4pf deposits. Generally EU7pf thins and thickens in the opposite sense to the underlying EU4pf deposits, but in some places just mantles EU4pf (Figure 8c). In general, the thickness decreases toward the northeast and south, where EU7pf disappears outside of the ruins to the south (Figure 12a). This deposit lacks any building fragments, but is characterized by mainly lithic lapilli; generally larger than the pumice lapilli (Figure 12b). EU7pf is mainly composed of a massive facies. Only in the north west sector does it show a crudely stratified-to-cross-bedded facies (Figure 12c). In this case, the variation in thickness is apparent in both the massive and accretionary lapilli facies (Figure 12c). The cohesive and extremely fine-grained character of these deposits does

not permit high-quality grain size analyses. Thus only a few samples could be analyzed, from which it is difficult to extract any general trends (Figures 12d and 12e). However, at sites 2c and 11a where disturbed EU4pf environments were encountered, the deposits of EU7pf did not show strong variations (Figures 12b, 12c, 12d, and 12e). EU8 comprises an alternation of normally graded, ashy bed sets, each up to 10 cm thick (Figure 8c). Each bed set is characterized at its base by a massive to crudely stratified facies overlain by accretionary lapilli facies. Extremely localized variations in thickness were observed for some of the massive or crudely stratified facies (site 8a, Figure 8c).

[24] EU7pf has been interpreted in the same way as EU4pf [Cioni *et al.*, 1992]. That is, it was emplaced by a sustained, turbulent, stratified PDC that transported and deposited sediment in the style of a high-density turbidity current [Cioni *et al.*, 2004]. The EU7pf parent current was



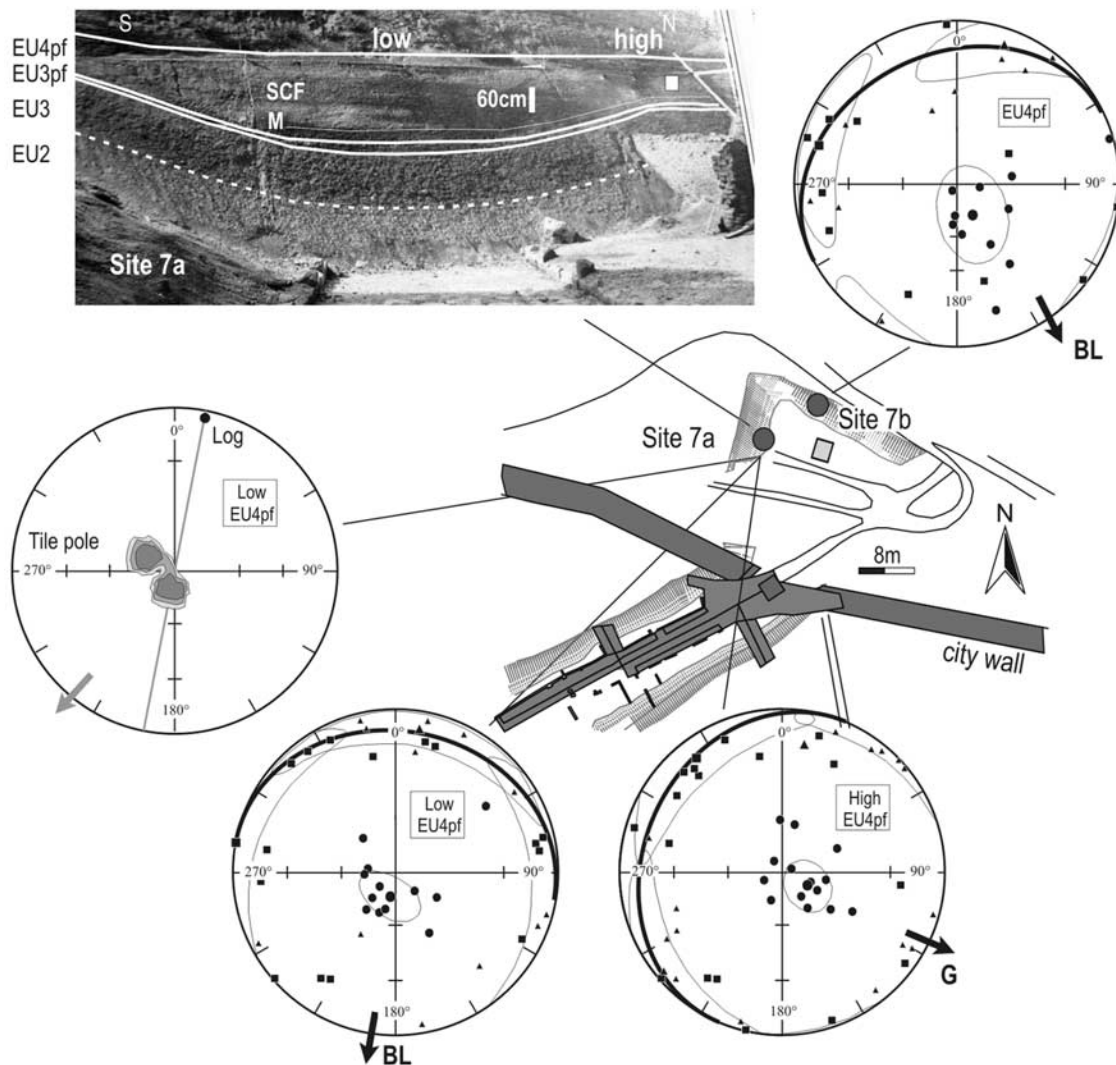


**Figure 14.** Variations in EU4pf flow directions across the road (topographic low) and the restraining wall (morphological high), as well as along the road at Porta di Nola site. For each sampled sections (dots in the sketch) the stereographic projection of AMS (symbols are as in Figure 3) are given. Bold letters close to the arrows refers to the color in Figure 6 (BL, blue; G, hollow). For site 7a the photo of the deposits (symbols of the facies as in Figure 5) and macroscopic indicators (symbols as in Figure 3) are also given. For site 7a (morphological low), magnetic foliation, tree log direction, and tile poles are concordant with a south-southwest flow direction perpendicular to the road direction. The magnetic lineation is dispersed within the magnetic foliation plane. For site 7a (morphological high), EU4pf data indicate a direction parallel to the road, and the magnetic lineation is along the maximum slope of the foliation plane. Site 7b is similar to 7a high. Photo courtesy of Soprintendenza di Pompeii.

less energetic than that of EU4pf, as indicated by its more rapid variations in thickness and grain size deposits away from the vent [Cioni *et al.*, 1992]. The facies associations at Pompeii indicate deposition during the final, waning stages of the current. This is also indicated by the lack of deposition just 200 m south of the town (site 26, Figure 12a). The variation in thickness of the accretionary lapilli facies indicates a major lateral component to the trailing upper current, from which this layer was emplaced. EU8 has been interpreted as deposited from low concentration, turbulent currents, in which the accretionary lapilli-bearing layers (facies AL) were derived from settling of particles from

the trailing ash clouds [Cioni *et al.*, 1992, Gurioli *et al.*, 2002]. The presence of several layers (Figure 8c) suggests that these deposits were emplaced by a number of phreatomagmatic pulses that characterized the final stages of the eruption [Cioni *et al.*, 1992]. As with EU7pf, the massive to crudely stratified facies of EU8 at the Pompeii site are suggestive of emplacement during the final stages of waning flow. For EU8, the down-current deposition is formed by fall-out of ash from a stagnant suspension in which the kinetic energy is not high enough to exert high shear stress on the bed [Chough and Sohn, 1990]. In general, the EU7pf and EU8 deposits mantled a town that had already been



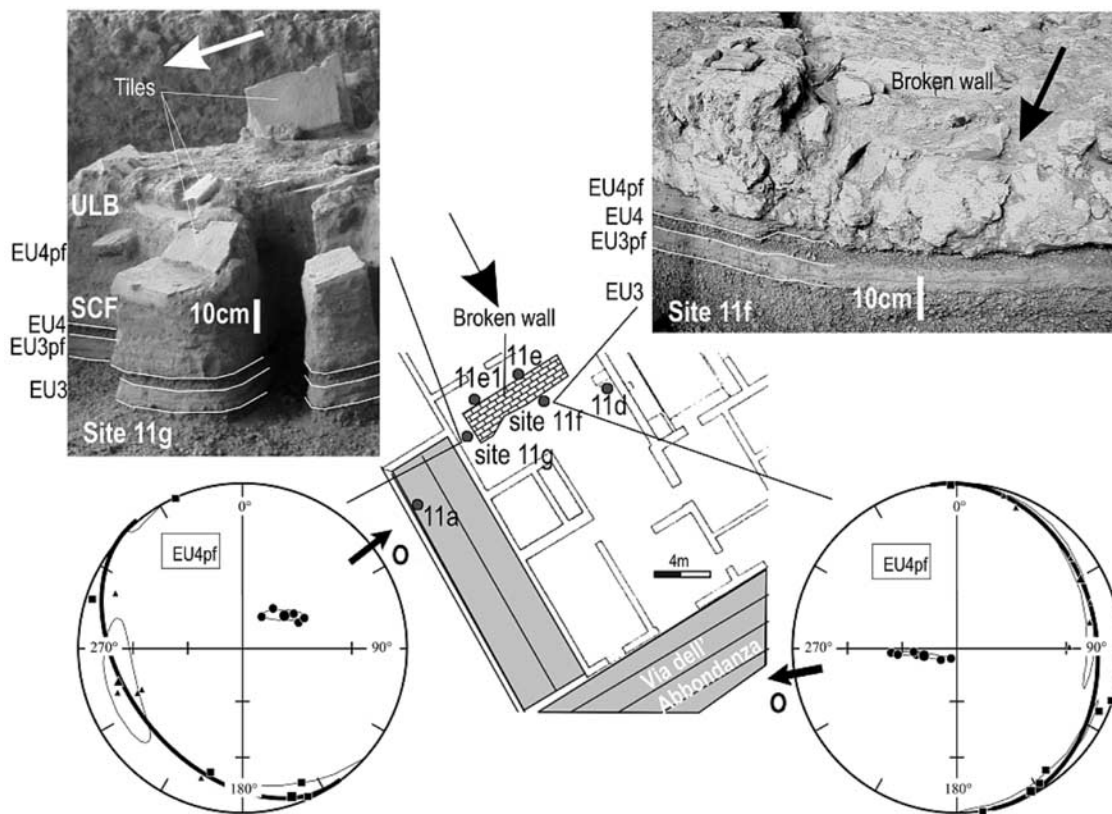


**Figure 15.** Variation in EU4pf flow direction inside a room of Casti Amanti House. For each sampling site (dots in the sketch) the photo of the deposits (symbols of the facies are as in Figure 5) and the stereographic projection of AMS (symbols as in Figure 3) are given. Bold letters close to the arrows refers to the color in Figure 6 (O, orange). The AMS directions are well defined, with the magnetic lineation perpendicular to the inferred direction. The interaction is very strong and the directions are completely disturbed.

severely damaged by the preceding currents (mainly EU4pf). Consequently, EU7pf and EU8 only show rare variations in thickness. These are related to the very low amplitude topography left by the previous deposits (site 8a, Figure 8c).

## 6. Integration of AMS and Sedimentological Data

[25] Both the AMS and sedimentological data show that the presence of the town strongly affected the flow directions of, and deposition from, those PDCs that reached and entered it. To illustrate how the integrated AMS and sedimentological data reveal the influence of the town on the emplacement of the PDC deposits, a particular study of EU4pf deposits was made. This was performed at four case-type outcrops: site 2 (Figure 13), site 7 (Figure 14), site 11 (Figure 15), and sites 24 and 14 (Figure 16). At site 2 a large, luxurious suburban villa (Villa dei Misteri) was located NW of Pompeii (Figure 1b). Upflow of and around the villa the EU4pf fabric is well developed (sites 2a and 2b, Figure 13). Both magnetic foliation and lineation are imbricated upflow; their azimuths coincide and are consistent with the direction of the tree logs found at site 2a and concordant with the main flow direction. However, along the northeastern side of the villa (site 2b), the orientation of the walls was slightly different to that of the main flow

and the AMS inferred flow orientation matches that of the walls. The high walls of the villa that at the time of the flow, were still protruding 2–3 m above the surface of the fallout deposits, were thus able to divert the lower part of the current while forcing no substantial change in the sedimentation process as the fabric geometry did not change. Downflow of the villa (site 2c, Figure 13), the vertical facies association consists of two facies: a massive, building debris-rich lower portion, followed by undulatory lenticular bedded deposits. Both the directions inferred from tiles and magnetic foliation are opposite to that of the main flow, and the magnetic lineation is dispersed within the foliation plane being, in some specimens, orthogonal to the main flow direction. In this case, the walls of the villa were overridden by the current that experienced a decoupling between the lower part, which was able to interact with the walls, and the upper part, which was unaffected. Following *Gurioli et al.* [2005], the upflow-oriented magnetic direction can be explained by generation of a vortex in the wake of a bluff with a nonzero incidence angle of the main flow relative to the building. At site 7 (Figure 14), the deposits fill a road and drape the restraining walls (morphological low and highs, respectively) which trend parallel to the city walls, oriented here at  $110^\circ$  (map in Figure 14). The lineation is dispersed within the foliation plane in all samples, a feature interpreted as being due to turbulence [e.g., *Cagnoli and*

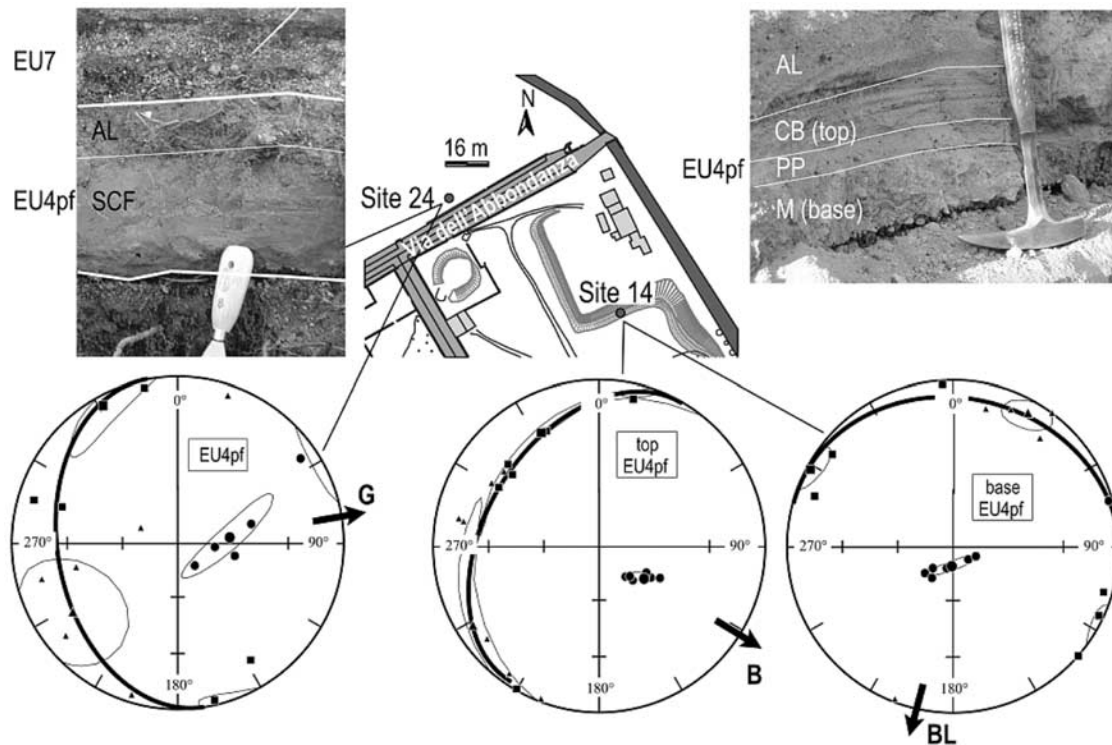


**Figure 16.** Variation in EU4pf flow direction on two paleohighs close to the east end of Via dell'Abbondanza. For each sampling site (dots in the sketch) the photo of the deposits (symbols of the facies are as in Figure 5) and the stereographic projection of AMS (symbols are as in Figure 3) are given. Bold letters close to the arrows refers to the color in Figure 6 (G, hollow; B, black; BL, blue). For site 24, EU4pf inferred direction is deflected along the road and perpendicular to the main flow direction with the magnetic lineation perpendicular to the inferred direction. Site 14 EU4pf base and EU4pf top show two different directions and magnetic behaviors. At the base the direction is deflected with the magnetic lineation perpendicular to the inferred direction, while at the top is consistent with the main flow direction.

Tarling, 1997; Ort *et al.*, 2003]. The magnetic foliation is well developed and strongly affected by the morphology. The samples collected on top of the restraining walls (site 7a\_high, Figure 14) are characterized by a well developed foliation whose imbrication yields a flow direction parallel to the city walls, similar to sites 5 and 6 (Figure 6). The lineation shows some dispersion, but the mean imbrication and azimuth for this site agree with those of the foliation. In this case, the lower part of the current was diverted by the city walls with little or no disturbance in sedimentation. In contrast, on the road (at site 7a\_low, Figure 14), the magnetic foliation and the tile attitudes, match the orientation of the walls-to-road slope. In addition, the highly dispersed lineation is orthogonal to the main flow direction. It is inferred that a turbulent lower part of the current became trapped in the road and filled it. The flow direction inferred at site 7b, a few meters northeast of the road (on the other side of the wall), is halfway between the two different directions found at site 7a, high and low. It can tentatively be interpreted as representing a transition between the two different regimes. The deposits at site 11 (Figure 1b, inside a room of Casti Amanti house) were sampled around a wall (sites 11e, 11e1, 11f and 11g, Figure 15) that collapsed during the passage of the dense, basal portion of EU4pf [Dal Maso *et al.*, 1999; Cioni *et al.*,

2000; Luongo *et al.*, 2003a]. The main flow direction, as indicated by the orientation of the knocked down wall, was probably from NW. The deposits upflow from the broken wall do not show the normal grading pattern of EU4pf found everywhere else (site 11e, Figures 11 and 15). In addition, the base of EU4pf at site 11e is poor in lapilli when compared with the other deposits at the left edge of the wall (site 11e1, Figures 11 and 15) and those downflow of the wall (sites 11g and 11f, Figures 11 and 15). These sedimentological features suggest that upflow of the wall the parental current was erosive and did not emplace a coarse-grained basal unit, but deposited only its upper, finer-grained portion. In the sites at the edge of and downflow of the wall (sites 11e1, 11f and 11g, Figure 15), the current regained its internal stratification and sedimented the coarse-grained basal portion once again (Figures 11a and 11b). However, the facies association described for these deposits (sites 11f and 11g, Figure 10c) indicates a turbulent environment in which deposition took place. This conclusion is further substantiated by the characteristics of the magnetic fabric that show a lineation dispersed along the foliation plane and roughly orthogonal to its imbrication. This is typical of turbulence. Furthermore, the derived flow directions were related to the lower part of the current that operated around the wall and was completely decoupled from the northwest to southeast moving upper

**Table 6.** Urban Fabric Data for Ancient Pompeii and Modern Pompeii<sup>a</sup>

	$A_T$ , km <sup>2</sup>	$A_P$ , km <sup>2</sup>	$A_F$ , km <sup>2</sup>	$H_b$ , m	$\Delta H_b$ , m	$\lambda_f$	$\lambda_p$	$z_0$ , m	$d$ , m
Ancient Pompeii	0.54	0.48	0.53	3.6	1.6	0.998	0.89	0.5	3.7
Modern Pompeii downtown	0.51	0.16	0.14	9.4	5.4	0.27	0.31	1.4	7.3
Modern Pompeii municipality	12.42	1.98	0.86	6.1	3.7	0.07	0.16	0.4	1.6

<sup>a</sup>See Figure 17 for the location. Symbols [after *Britter and Hanna, 2003*] are  $A_T$ , building lot area;  $A_P$ , total building plan area;  $A_F$ , total building frontal area;  $H_b$ , building height;  $\Delta H_b$ , standard deviation;  $\lambda_f = D_f/D_T$ ,  $\lambda_p = D_f/D_T$ ;  $z_0$ , roughness length;  $d$ , surface displacement length.

current. Sites 24 and 14 comprise two outcrops along (site 24) and close to (site 14) Via dell'Abbondanza (Figure 16). At site 24, the derived flow directions indicate that EU4pf moved along the road within the city (sites 10 and 12c, Figure 6). At site 14 (Figure 16), the EU4pf base deposit is represented by a massive facies, whereas the top shows a plane-parallel to cross-bedded facies. The base and top also show two different directions and magnetic behaviors. At the top, the direction trends parallel to the main walls and roads, a direction perpendicular to that encountered in the road at site 24, and the lineation azimuth is consistent with the imbrication of magnetic foliation. At the base, the flow direction is deflected, and the lineation azimuth is orthogonal to the flow. Thus, even in a very thin deposit whose sedimentary features indicate deposition from a current with a stable internal stratification, the basal portion is heavily influenced by the roughness of the surface over which it is moving. In contrast the stratified facies seems to be more coupled with the overlying upper current.

## 7. Urban Fabric Influences on PDC Directions and Emplacement

[26] The interactions between the PDCs and Pompeii, as described above, have been quantified using the geometrical, textural, sedimentary structure and fabric variations observed in the A.D. 79 deposits. Next, the urban fabric of the town and how it was able to disturb the PDCs will be discussed. *Esposti Ongaro et al. [2002]* have already shown that urban obstacles exert large drag forces on pyroclastic density currents. By analogy with the atmospheric boundary layer, which has a thickness that is generally greater than the mean building height,  $H_b$ , the interaction of a PDC with a town can be better understood. *Grimmond and Oke [2002]* outlined three major sublayers in the atmospheric boundary layer over an urban area. The lowermost is the urban canopy sublayer. Within this layer flow, at a specific point, is directly affected by local obstacles. The second layer, the roughness sublayer, is a layer within which the flow is still adjusting to the effects of urban obstacles. Within the final layer, the inertial sublayer, the boundary layer has adapted to the integrated effect of the underlying urban surface. Similar behavior is expected for the pyroclastic density current and the wind near-surface shear stress and velocity profiles. However, it seems that this analogy is applicable to a single current encountering a city, and becomes less

applicable as more deposits gradually fill in the topography. Surface shear stress and wind profiles are usually parameterized by introducing two scaling lengths:  $z_0$  (the surface roughness length) and  $d$  (the surface displacement length) [*Britter and Hanna, 2003*]. *Davenport et al. [2000]* directly related  $z_0$  and  $d$  to urban/industrial land use and outlined five main categories. The first ( $z_0 = 0.1$  m) is appropriate for moderately open country with occasional obstacles, at relative separations that are at least  $20 H_b$ . The second ( $z_0 = 0.25$  m) is a rough surface comprising scattered buildings and/or industrial obstacles at relative separations of 8 to  $12 H_b$ . The third ( $z_0 = 0.5$  m) is a very rough surface comprising an area of moderate coverage of low buildings and/or industrial tanks at relative separations of 3 to  $7 H_b$ . The fourth ( $z_0 = 1.0$  m) considers skimming flow in a densely built-up area without much obstacle height variation. The final case ( $z_0 = 2.0$  m) is chaotic and is appropriate for city centers with a mixture of low-rise and high-rise buildings.

[27] For Pompeii, estimates of  $z_0$  and  $d$  can be made using information about building size and spacing. The total building plan area,  $A_P$ , and the total building frontal area,  $A_F$ , in a building lot of area  $A_T$  can be used to define the “lambda parameters.” These are used in many empirical urban boundary layer formulas:  $\lambda_p = A_P / A_T$ ,  $\lambda_f = A_F / A_T$ . We have used the approach of *Hanna and Britter [2002]*, who considered several field and laboratory data sets as well as theoretical formulas in the literature, to evaluate flow behavior in ancient Pompeii using these lambda parameters as well as  $z_0$  and  $d$  (Table 6). We note also that in ancient Pompeii, all the roofs had already collapsed when the PDCs arrived so that just walls were surviving at the time of EU3pf and EU4pf emplacement.

[28] For ancient Pompeii, we obtain  $\lambda_f$  of  $\sim 1$ , where roof collapse increased the number of walls exposed to the flow. The ancient city also presented a closely packed urban settlement where the city area contained a dense rectangular mesh of orthogonal streets. This resulted in a high ratio of building plan to lot area ( $\lambda_p = 0.89$ ). Because of relatively low and uniform building heights (average wall height being  $3.6 \pm 1.6$  m), the ancient town is expected to have exerted a moderate/high drag force on the flow. We obtain  $z_0 \sim 0.5$  m, a value considered to fall in the “very rough” category of *Davenport et al. [2000]*. Locally  $z_0$  values of  $\sim 1$  m are estimated so that in principle, a skimming flow may be expected to develop locally. This did indeed occur, as confirmed by reverse flow directions in the lower, depositional regime of EU4pf deposits. In addition, the drag force was increased by the hill on which ancient Pompeii was located and by the high particle concentration in the basal portion of the current. These results confirm that the lower part of EU4pf current interacted with the town, but, as expected, the thicker, upper current by-passed these obstacles. The urban canopy also encouraged deposition so that the current lost some of its load, as suggested by the finer-grained, thinner deposits apparent downflow of Pompeii (Figure 10).

## 8. Discussion

[29] Across ancient Pompeii, sedimentological features of the EU3pf and EU4pf deposits show that the parent currents, even those that were able to emplace only thin ash



layers, were stratified in terms of density, grain size and velocity. These currents were capable of interacting with the urban topography and their behavior, as observed in Herculaneum [Gurioli *et al.*, 2002], varied mainly as a function of obstacle height and density stratification within the current. Other authors report qualitative data that describe partial flow blocking and diversion of lower, denser parts of the flow by human infrastructure [e.g., Valentine, 1998; Luongo *et al.*, 2003a; Baxter *et al.*, 2005]: a phenomenon that is confirmed and quantified here. EU3pf was locally sensitive to obstacles of a few decimeters in height, suggesting that its denser, thin lower part was capable of only filling minor depressions. This lower layer was overlain by a thicker, more diluted, upper part that was unaffected by such obstacles. For 10-cm-deep depressions the whole deposit shows variation in thickness, grain size and sedimentary structure. However, these variations were locally controlled, being short-lived and of limited extent, as suggested by the generally constant thickness and grain size of the deposits across the town (Figure 9). These features suggest that the very diluted, upper part of the current was able to feed a constant sediment supply to the lower current, as already observed for large-scale currents [e.g., Fisher, 1990; Dade, 2003; Browne and Gardner, 2005]. EU4pf was able to interact with obstacles of a few meters in height, showing the most efficient interaction with the town. The AMS data suggest that the main structures (i.e., the city walls and the road network) were able to divert the flow without substantially modifying its depositional characteristics. Instead, 2- to 4-m-high features (positive or negative) could both divert the flow and interact with the lower current, strongly changing the sedimentary structures, texture and fabric of the emplaced deposits. Increases in turbulence, due to these irregularities, are evident from upstream particle orientations which develop downflow of obstacles, or inside cavities (Figure 6). These are also evident from characteristic sedimentary structures such as undulatory lenticular bedded facies on the lee side of the obstacles (Figures 8b and 10c). All of these features can be interpreted as resulting from the capability of this current to form vortices downslope of obstacles [Gurioli *et al.*, 2005]. In contrast the dilute, upper part of the current was able to flow over the town [Luongo *et al.*, 2003a, 2003b; Gurioli *et al.*, 2005]. However, the decrease in thickness and grain size of the EU4pf deposits across the town indicates that the upper portion of the current was not able to fully restore the sediment supply to the lower current. This is in agreement with the high roughness of the urban canopy, which encouraged deposition, but was not able to stop the current. The EU4pf lower current seems to have been 2–4 m thick, as indicated by the scale of the objects with which it interacted. Above this layer, a transitional zone occurs that can be more or less coupled with the transport system. This is very clear from the AMS results at site 14 (Figure 16) where the massive and stratified facies seem decoupled; the former being strongly influenced by the ground, while the latter show flow directions more consistent with that of the upper current. These results confirm what has already been observed at larger scales in ignimbrite deposits [e.g., Suzuki and Ui, 1982; Baer *et al.*, 1997; Ort *et al.*, 1999, 2003] and are in agreement with the disturbance exerted by the hill and the town on the current. The mantle-bedded ash

layers from EU7pf and EU8 were most likely formed by fallout of ash from a slow moving, turbulent current. At this point, all small irregularities with which they could interact where more-or-less buried. Instead all that was left were the large irregularities (e.g., the city walls and towers), which were too large to disturb the deposition. Thus EU7pf and EU8 simply mantled a town whose small-scale irregularities had mostly been buried and smoothed by the EU4pf deposits.

[30] Should such flows enter modern Pompei (Figure 17), the impact will be even more serious. Today, the municipality of Pompei extends over 12.4 km<sup>2</sup> and has ~26,000 inhabitants. The average building height is  $6.1 \pm 3.7$  m and  $z_0$  is ~0.4 m, characteristic of an area of moderate low building and industrial unit coverage (Figure 16 and Table 6). In contrast, the downtown area of modern Pompei comprises a mixture of low- and high-rise buildings (average wall height being  $9.4 \pm 5.4$  m). In such a setting, dilute currents, like EU3pf, EU7pf and EU8, will interact with very small irregularities, mainly running undisturbed through the town. For less diluted currents, such as EU4pf, a chaotic flow is expected to occur, where long wakes form downflow from tall buildings to interact with successive tall buildings and adjacent smaller ones [Britter and Hanna, 2003]. In addition, the increased variability in building height across modern Pompei would exert a stronger drag force ( $z_0 \sim 1.4$ ), encouraging vortex formation, deceleration and deposition. This is consistent with simulations of pollutant dispersion in streets that show that obstacles, such as buildings, facilitate the formation of vortices and, consequently, lead to local increases in pollutant concentration, especially when there are higher buildings downstream [Xia and Leug, 2001].

## 9. Conclusions

[31] The integration of field data and AMS measurements has allowed the behavior of turbulent PDCs moving through an urban area to be constrained. Both dilute (EU3pf, EU7pf, and EU8) and less dilute (EU4pf) currents of the A.D. 79 eruption of Vesuvius were stratified and able to partially or fully interact with the town of Pompeii. In the case of EU3pf, EU7pf, and EU8 the interaction with structures was minimal, and the town did not affect the upper part of these currents, which were able to restore the sediment supply to the depositional regime. The currents were thus able to engulf the town without inflicting serious damage on the structures. However, their temperatures and particle concentrations still made them extremely hazardous to humans [Cioni *et al.*, 2000; Zanella *et al.*, 2007]. In contrast, EU4pf had a significant impact, seriously damaging many structures. This current, having a scale of the same vertical dimension as the urban roughness, experienced the most interaction with the town. Even if the town was able to exert a strong drag force on the current, as revealed by the decrease in thickness and grain size in the emplaced deposits across and downflow from the town, the urban fabric was not able to stop it. The closely spaced arrangement of ancient Pompeii, its average roughness and the many openings (left by roof collapse and windows) helped the upper and lower parts of the current to decouple. This allowed its lower part to follow the city walls and the

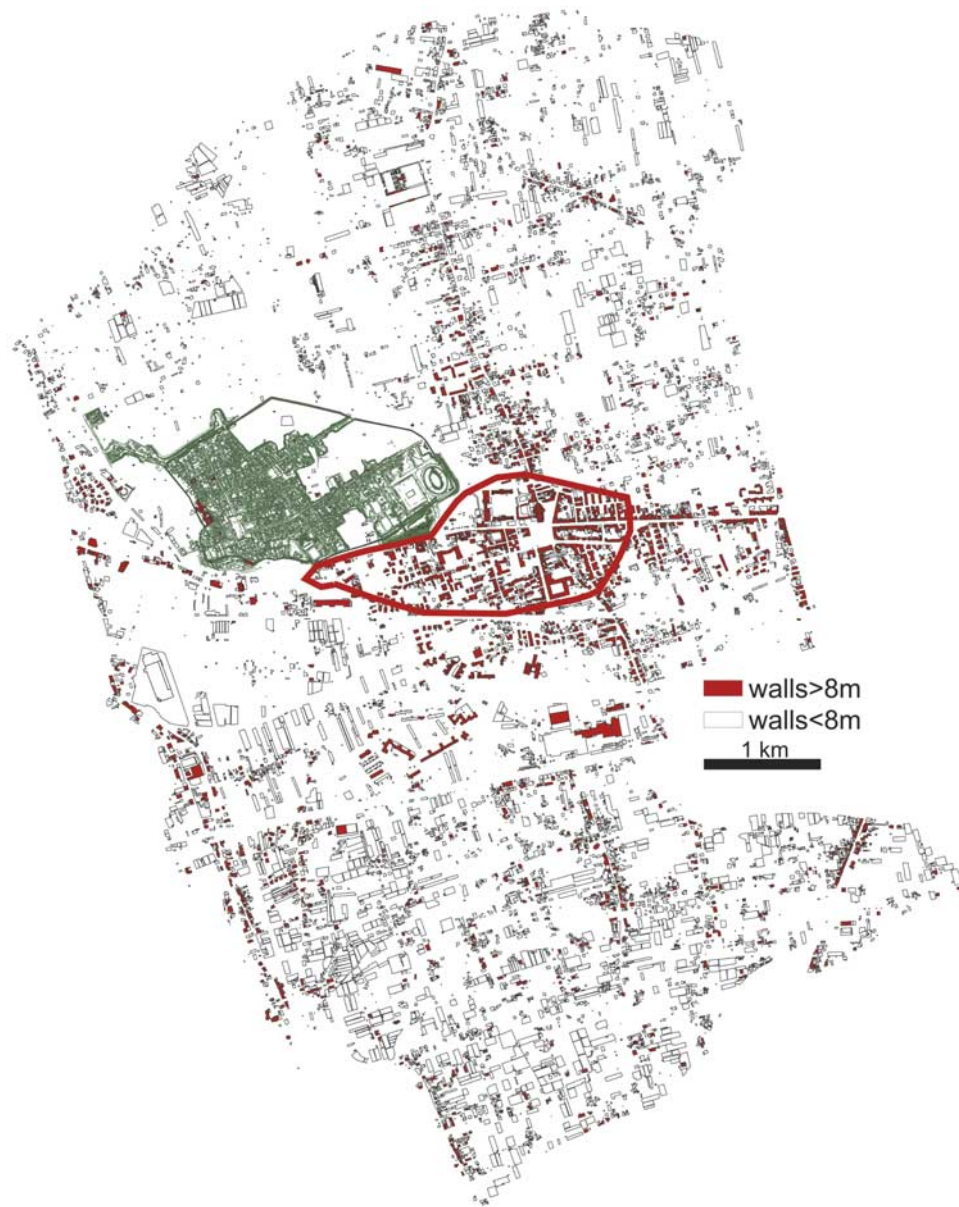


**Figure 17.** Modern Pompei Municipality showing ancient Pompeii (in green) and the limits of modern Pompei downtown (delimited by bold red line). Buildings with wall heights of less than 8 m are given in white and wall heights of greater than 8 m are given in red.

intracity roads, to enter all the cavities to form vortices and to be, locally, extremely erosive.

[32] In summary, the degree of interaction between a town and a current moving through it depends on the thickness of the lower, dense part of the current. Only topography with similar scale will increase turbulence or encourage deposition in the current. However, given a minimum thickness of  $\sim 30$  m for the total thickness of very dilute currents during the A.D. 79 eruption (based on their capability to override the 30-m-high paleotopography of Pompeii) and 200 m for EU4pf [Gurioli, 2000], the town, with local maximum elevations of just 7 m, had no capability at all to block such currents.

[33] Given the present urban fabric surrounding Vesuvius, the degree of interaction between any similar PDCs and the urban fabric would now be increased; a result of the huge number of buildings and their heterogeneous sizes and shapes today. Dilute currents can only be blocked, locally, by excessively tall ( $>30$  m high) buildings (i.e., buildings that are taller than the total current thickness). Generally, however, dilute currents will move through an urban area largely undisturbed; interactions occurring only with objects at the decimeter scale. For less dilute currents, like EU4pf, chaotic flow is expected to interact with successive tall buildings and adjacent smaller ones, forming vortices and unpredictable flow paths. In conclusion it seems that a town



will never be able to stop a current. However, under certain conditions some diversion is possible, as well as modification of the current load, with the degree of interaction with the urban fabric decreasing with increased dilution.

[34] **Acknowledgments.** We are indebted to P. G. Guzzo, G. Stefani, A. d'Ambrosio, A. Varone, and C. Cicirelli for archaeological assistance; G. Di Martino, B. Di Martino, and A. Cataldo for their logistic help in the archaeological sites; and B. F. Houghton and A. J. Harris for informal review. We thank A. L. Grunder, D. Tarling, and M. Ort for their thoughtful and constructive reviews. We deeply thank S. Ranieri for the logistic and field assistance as well as for the stimulating discussions we had in the field. We thank C. Frola and E. Deluca for AMS measurements and their help in the field and Marina Bisson for the GIS database of Pompeii and Figure 17. A. J. Harris, E. Tema, and M. Lanfranco contributed to field work. This work was partially supported by the European Commission, Project Exploris EVR1-CT-2002-40026 and the financial support of INGV and University of Turin.

## References

- Allen, J. R. L. (1984), *Sedimentary Structures: Their Character and Physical Basis*, Elsevier, New York.
- Baer, E. M., R. V. Fisher, M. Fuller, and G. Valentine (1997), Turbulent transport and deposition of the Ito pyroclastic flow: Determinations using anisotropy of magnetic susceptibility, *J. Geophys. Res.*, **102**, 22,565–22,586.
- Barberi, F., R. Cioni, M. Rosi, R. Santacroce, A. Sbrana, and R. Vecci (1989), Magmatic and phreatomagmatic phases in explosive eruptions of Vesuvius as deduced by grain-size and compositional analysis of pyroclastic deposits, *J. Volcanol. Geotherm. Res.*, **38**, 287–307.
- Barberi, F., G. Macedonio, M. T. Pareschi, and R. Santacroce (1990), Mapping the tephra fallout risk: An example from Vesuvius (Italy), *Nature*, **344**, 142–144.
- Bardot, L. (2000), Emplacement temperature determinations of proximal pyroclastic deposits on Santorini, Greece, and their implications, *Bull. Volcanol.*, **61**, 450–467.
- Bardot, L., and E. McClelland (2000), The reliability of emplacement temperature estimates using palaeomagnetic methods: A case study from Santorini, Greece, *Geophys. J. Int.*, **143**, 39–51.
- Baxter, P. T., A. Neri, and M. Todesco (1998), Physical modeling and human survival in pyroclastic flows, *Nat. Hazard*, **17**, 163–176.
- Baxter, P. J., R. Boyle, C. Paul, A. Neri, R. Spence, and G. Zuccaro (2005), The impacts of pyroclastic surges on buildings at the eruption of the Soufriere Hills volcano, Montserrat, *Bull. Volcanol.*, **67**, 292–313.
- Blong, R. J. (1984), *Volcanic Hazards: a Sourcebook on the Effects of Eruptions*, Elsevier, New York.
- Branney, M. J., and P. Kokelaar (2002), Pyroclastic density currents and the sedimentation of ignimbrites, *Geol. Soc. London Mem.*, **27**, 143 pp.
- Britter, R. E., and S. R. Hanna (2003), Flow and dispersion in urban areas, *Annu. Rev. Fluid Mech.*, **35**, 469–496.
- Browne, B. L., and J. E. Gardner (2005), Transport and deposition of pyroclastic material from the 1000 A. D. caldera-forming eruption of Volcán Ceboruco, Nayarit, Mexico, *Bull. Volcanol.*, **67**, 469–489.
- Bryan, J. E., R. A. F. Cas, and J. Martí (1998), Lithic breccias in intermediate volume phonolitic ignimbrites, Tenerife (Canary Islands). Constraints on pyroclastic flow depositional processes, *J. Volcanol. Geotherm. Res.*, **81**, 269–296.
- Cagnoli, B., and D. H. Tarling (1997), The reliability of anisotropy of magnetic susceptibility (AMS) data as flow direction indicators in friable surge and ignimbrite deposits: Italian examples, *J. Volcanol. Geotherm. Res.*, **75**, 309–320.
- Carey, S., and H. Sigurdsson (1987), Temporal variations in column height and magma discharge rate during the 79 AD eruption of Vesuvius, *Geol. Soc. Am. Bull.*, **99**, 303–314.
- Cas, R. A. F., and J. V. Wright (1987), *Volcanic Successions*, CRC Press, Boca Raton, Fla.
- Chough, S. K., and Y. K. Sohn (1990), Depositional mechanics and sequences of base surges, Songaksan tuff ring, Cheju Island, Korea, *Sedimentology*, **37**, 1115–1135.
- Cioni, R., P. Marianelli, and A. Sbrana (1992), Dynamics of the AD 79 eruption: Stratigraphic, sedimentological and geochemical data on the successions of the Somma-Vesuvius southern and eastern sectors, *Acta Volcanol.*, **2**, 109–123.
- Cioni, R., A. Sbrana, and L. Gurioli (1996), The deposits of AD 79 eruption, in *Vesuvius Decade Volcano Workshop Handbook, International CEV-CMVD Workshop on Vesuvius, Sept 1996*, edited by R. Santacroce et al., pp. E1–E31, Cons. Natl. delle Ric., Rome, Italy.
- Cioni, R., L. Gurioli, A. Sbrana, and G. Vougioukalakis (2000), Precursory phenomena and destructive events related to the Late Bronze Age Minoan (Thera, Greece) and AD 79 (Vesuvius, Italy) Plinian eruptions: Inferences from the stratigraphy in the archaeological areas, in *The Archaeology of Geological Catastrophes*, edited by W. G. McGuire et al., *Geol. Soc. Spec. Publ.*, **171**, 123–141.
- Cioni, R., L. Gurioli, R. Lanza, and E. Zanella (2004), Temperatures of the A. D. 79 pyroclastic density current deposits (Vesuvius, Italy), *J. Geophys. Res.*, **109**, B02207, doi:10.1029/2002JB002251.
- Cole, P. D. (1991), Migration direction of sandwave structures in pyroclastic surge deposits: Implications for depositional processes, *Geology*, **19**, 1108–1111.
- Cole, P. D., J. E. Guest, and A. M. Duncan (1993), The emplacement of intermediate volume ignimbrite: A case study from Roccamonfina volcano, southern Italy, *Bull. Volcanol.*, **55**, 467–480.
- Dade, W. B. (2003), The emplacement of low-aspect ratio ignimbrites by turbulent parent flows, *J. Geophys. Res.*, **108**(B4), 2211, doi:10.1029/2001JB001010.
- Dal Maso, C., A. Marturano, and A. Varone (1999), Pompei, il racconto dell'eruzione, *Scienze*, **371**, 58–65.
- Davenport, A. G., C. S. B. Grimmond, T. R. Oke, and J. Weiranga (2000), Estimating the roughness of cities and scattered country, paper presented at 12th Conference on Applied Climatology, Am. Meteorol. Soc., Ashville, N. C.
- Dellino, P., and L. La Volpe (2000), Structures and grain size distribution in surge deposits as a tool for modelling the dynamics of dilute pyroclastic density currents at La Fossa di Vulcano (Aeolian Islands, Italy), *J. Volcanol. Geotherm. Res.*, **96**, 57–78.
- Dobran, F., A. Neri, and M. Todesco (1994), Assessing the pyroclastic flow hazard at Vesuvius, *Nature*, **367**, 551–554.
- Druitt, T. H. (1992), Emplacement of the 18 May 1980 lateral blast deposit east-northeast of Mount St. Helens, Washington, *Bull. Volcanol.*, **54**, 554–572.
- Druitt, T. H. (1998), Pyroclastic density current, in *The Physics of Explosive Volcanic Eruptions*, edited by J. S. Gilbert and R. S. J. Sparks, *Geol. Soc. Spec. Publ.*, **145**, 145–182.
- Ellwood, B. B., and M. T. Ledbetter (1977), Antarctic bottom water fluctuations in the Vema Channel: Effects of velocity changes on particle alignment and size, *Earth Planet. Sci. Lett.*, **35**, 189–198.
- Elston, W. E., and E. I. Smith (1970), Determination of flow direction of rhyolitic ash-flow tuffs from fluidal textures, *Geol. Soc. Am. Bull.*, **81**, 3393–3406.
- Esposti Ongaro, T., A. Neri, M. Todesco, and G. Macedonio (2002), Pyroclastic flow hazard assessment at Vesuvius (Italy) by using numerical modeling. II. Analysis of flow variables, *Bull. Volcanol.*, **64**, 178–191.
- Fisher, R. V. (1990), Transport and deposition of a pyroclastic surge across an area of high relief: The 18 May 1980 eruption of Mount St. Helens, Washington, *Geol. Soc. Am. Bull.*, **102**, 1038–1054.
- Fisher, R. V., and H. U. Schmincke (1984), *Pyroclastic Rocks*, Springer, New York.
- Folk, R. L., and W. C. Ward (1957), Brazos river bar: A study in the significance of grain-size parameters, *J. Sediment. Petrol.*, **27**, 3–26.
- Freundt, A., and M. I. Bursik (1998), Pyroclastic flow transport mechanism, in *From Magma to Tephra: Modelling Physical Processes of Explosive Volcanic Eruptions*, edited by A. Freundt and M. Rosi, pp. 173–246, Elsevier, New York.
- Giannini, F., M. T. Pareschi, G. Stefani, and M. Bisson (2000), The ancient and the new Pompeii: A project for the monitoring of archaeological sites in densely populated areas, in *Beyond the Map*, edited by G. Lock, 187–198, IOS Press, Amsterdam.
- Gray, E. G., J. Alexander, and M. R. Leeder (2005), Quantifying velocity and turbulence structure in depositing sustained turbidity currents across breaks in slope, *Sedimentology*, **52**, 467–488.
- Grimmond, C. S. B., and T. R. Oke (2002), Turbulent heat fluxes in urban area: Observation and a local-scale urban meteorological parameterisation scheme, *J. Appl. Meteorol.*, **41**, 792–810.
- Gurioli, L. (2000), Pyroclastic flow: Classification, transport and emplacement mechanisms, *Plinius*, **23**, 84–89.
- Gurioli, L., R. Cioni, and C. Bertagna (1999), I depositi di flusso piroclastico dell'eruzione del 79 d.C.: Caratterizzazione stratigrafica, sedimentologica e modelli di trasporto e deposizione, *Atti Soc. Tosc. Sci. Nat. Mem., Ser. A*, **106**, 61–72.
- Gurioli, L., R. Cioni, A. Sbrana, and E. Zanella (2002), Transport and deposition of pyroclastic density currents over an inhabited area: The deposits of the AD 79 eruption of Vesuvius at Herculaneum, Italy, *Sedimentology*, **49**, 929–953.
- Gurioli, L., M. T. Pareschi, E. Zanella, R. Lanza, E. Deluca, and M. Bisson (2005), Interaction of pyroclastic currents with human settlements: Evidences from ancient Pompeii, *Geology*, **33**, 441–444.

- Hanna, S. R., and R. E. Britter (2002), *Wind Flow And Vapor Cloud Dispersion at Industrial and Urban Sites*, Am. Inst. of Chem. Eng., New York.
- Hillhouse, J. W., and R. E. Wells (1991), Magnetic fabric, flow directions, and source area of the lower Miocene Peach Springs tuff in Arizona, California, and Nevada, *J. Geophys. Res.*, **96**, 12,443–12,460.
- Hughes, S. R., and T. H. Druitt (1998), Particle fabric in a small, type-2 ignimbrite flow unit (Laacher see, Germany) and implications for emplacement dynamics, *Bull. Volcanol.*, **60**, 125–136.
- Inman, D. L. (1952), Measures for describing the size distribution of sediments, *J. Sediment. Petrol.*, **22**, 125–145.
- Jelinek, V. (1977), *The Statistical Theory of Measuring Anisotropy of Magnetic Susceptibility of Rocks and Its Application*, 88 pp., Geofyzika, Brno, Czech Republic.
- Kamata, H., and K. Mimura (1983), Flow directions inferred from imbrication in the Handa pyroclastic flow deposit in Japan, *Bull. Volcanol.*, **46**, 277–282.
- Kent, D. V., D. Ninkovich, T. Pescatore, and R. S. J. Sparks (1981), Palaeomagnetic determination of emplacement temperature of Vesuvius AD 79 pyroclastic deposits, *Nature*, **290**, 393–396.
- Ledbetter, M. T., and B. B. Ellwood (1980), Spatial and temporal changes in bottom water velocity from the analysis of particle size and alignment in deep-sea sediments, *Mar. Geol.*, **38**, 245–261.
- Lirer, L., T. Pescatore, B. Booth, and G. P. L. Walker (1973), Two Plinian pumice-fall deposits from Somma-Vesuvius, Italy, *Geol. Soc. Am. Bull.*, **84**, 759–772.
- Lirer, L., R. Munno, P. Petrosino, and A. Vinci (1993), Tephrostratigraphy of the A. D. 79 pyroclastic deposits in perivolcanic areas of Mount Vesuvius (Italy), *J. Volcanol. Geotherm. Res.*, **58**, 133–139.
- Lowe, D. R. (1988), Suspended-load fallout rate as an independent variable in the analysis of current structures, *Sedimentology*, **35**, 765–776.
- Luongo, G., A. Perrotta, and C. Scarpati (2003a), Impact of the AD 79 eruption on Pompeii, I. Relations amongst the depositional mechanisms of the pyroclast products, the framework of the buildings and the associated destructive events, *J. Volcanol. Geotherm. Res.*, **126**, 201–223.
- Luongo, G., A. Perrotta, C. Scarpati, E. De Carolis, G. Patricelli, and A. Ciarallo (2003b), Impact of the AD 79 eruption on Pompeii, II. Causes of death of the inhabitants inferred by stratigraphic analysis and areal distribution of the human casualties, *J. Volcanol. Geotherm. Res.*, **126**, 169–200.
- MacDonald, W. D., and H. C. Palmer (1990), Flow directions in ash-flow tuffs: A comparison of geological and magnetic susceptibility measurements, Tshirege member (upper Bandelier tuff), Valles caldera, New Mexico, USA, *Bull. Volcanol.*, **53**, 45–59.
- Macedonio, G., M. T. Pareschi, and R. Santacroce (1988), A numerical simulation of the Plinian fall phase of 79 A.D. eruption of Vesuvius, *J. Geophys. Res.*, **93**, 14,817–14,827.
- McClelland, E. A., and T. H. Druitt (1989), Palaeomagnetic estimates of emplacement temperatures of pyroclastic deposits on Santorini, Greece, *Bull. Volcanol.*, **51**, 16–27.
- Nunziante, L., M. Fraldi, L. Lirer, P. Petrosino, S. Scotellaro, and C. Cicirelli (2003), Risk assessment of the impact of pyroclastic currents on the towns located around Vesuvius: A non-linear structural inverse analysis, *Bull. Volcanol.*, **65**, 547–561.
- Ort, M., M. Rosi, and C. D. Anderson (1999), Correlation of deposits and vent locations of the proximal Campanian Ignimbrite deposits, Campi Flegrei, Italy, based on natural remanent magnetization and anisotropy of magnetic susceptibility characteristics, *J. Volcanol. Geotherm. Res.*, **91**, 167–178.
- Ort, M., G. Orsi, L. Pappalardo, and R. V. Fisher (2003), Anisotropy of magnetic susceptibility studies of depositional processes in the Campanian ignimbrite, Italy, *Bull. Volcanol.*, **65**, 55–72.
- Palmer, H. C., and W. D. MacDonald (1999), Anisotropy of magnetic susceptibility in relation to source vents of ignimbrites: Empirical observations, *Tectonophysics*, **307**, 207–218.
- Postma, G., C. W. Nemec, and K. L. Kleinspehn (1988), Large floating clasts in turbidites: A mechanism for their emplacement, *Sediment. Geol.*, **105**, 71–93.
- Rees, A. I. (1983), Experiments on the production of a transverse grain alignment in a sheared dispersion, *Sedimentology*, **30**, 337–448.
- Schmincke, H. U., and D. A. Swanson (1967), Laminar viscous flowage structures in ash-flow tuffs from Gran Canaria, Canary Island, *J. Geol.*, **75**, 641–664.
- Sheridan, M. F., F. Barberi, M. Rosi, and R. Santacroce (1981), A model for Plinian eruptions of Vesuvius, *Nature*, **289**, 282–285.
- Sigurdsson, H., S. Cashdollar, and R. S. J. Sparks (1982), The eruption of Vesuvius in AD 79: Reconstruction from historical and volcanological evidence, *Am. J. Archaeol.*, **86**, 39–51.
- Sigurdsson, H., S. Carey, W. Cornell, and T. Pescatore (1985), The eruption of Vesuvius in 79 AD, *Natl. Geogr. Res.*, **1**, 332–387.
- Smith, G. A. (1986), Coarse-grained nonmarine volcanoclastic sediment: Terminology and depositional process, *Geol. Soc. Am. Bull.*, **97**, 1–10.
- Sohn, Y. K., and S. K. Chough (1989), Depositional processes of the Suwolbong tuff ring, Cheju Island (Korea), *Sedimentology*, **36**, 837–855.
- Suzuki, K., and T. Ui (1982), Grain orientation and depositional ramps as flow direction indicators of a large-scale pyroclastic flow deposit in Japan, *Geology*, **10**, 429–432.
- Tanguy, J. C., C. Ribiere, A. Scarth, and W. S. Tjetjep (1998), Victims from volcanic eruptions: A revised database, *Bull. Volcanol.*, **60**, 137–144.
- Ui, T., S. K. Kamata, R. Matsusue, K. Fujita, H. Metsugi, and M. Araki (1989), Flow behavior of large-scale pyroclastic flow. Evidence obtained from petrofabric analysis, *Bull. Volcanol.*, **51**, 115–122.
- Valentine, G. A. (1998), Damage to structures by pyroclastic flows and surges, inferred from nuclear weapons effects, *J. Volcanol. Geotherm. Res.*, **87**, 117–140.
- Xia, J., and D. Y. C. Leung (2001), A concentration correction scheme for Lagrangian particle model and its application in street canyon air dispersion modeling, *Atmos. Environ.*, **35**, 5779–5788.
- Zanella, E., L. Gurioli, G. Chiari, A. Ciarallo, R. Cioni, E. De Carolis, and R. Lanza (2000), Archaeomagnetic results from mural paintings and pyroclastic rocks in Pompeii and Herculaneum, *Phys. Earth Planet. Inter.*, **118**, 227–240.
- Zanella, E., L. Gurioli, M. T. Pareschi, and R. Lanza (2007), Urban fabric influences on pyroclastic density current at Pompeii (Italy): 2. Deposit temperature and hazard implications, doi:10.1029/2006JB004775, in press.

L. Gurioli, Geology and Geophysics, University of Hawaii, 1680 East-West Road, Honolulu, HI 96822, USA. (gurioli@hawaii.edu)

R. Lanza and E. Zanella, Dipartimento di Scienze della Terra, Università di Torino, Via Valperga Caluso 35, I-10125, Torino, Italy.

M. T. Pareschi, Istituto Nazionale di Geofisica e Vulcanologia, Via della Faggiola 32, I-56126, Pisa, Italy.